Investigating SuperCDMS SNOLAB Cosmogenic Background Spectra in Copper and Troubleshooting Production Cuts in Geant4

BY

Spencer Keller

A thesis submitted to the

Department of Physics

University of Toronto

in partial fulfillment of the requirements for the

Master of Science Degree

Option II

March, 2024

ABSTRACT

SuperCDMS SNOLAB is a planned dark matter direct detection experiment that aims to probe dark matter with masses below 10 GeV. It will use semiconducting silicon and germanium detectors cooled to $\sim$15 mk by a commercial dilution refrigerator to achieve thermal noise reduction. Nonetheless, the experiment is expected to observe a non-zero background rate originating from decay daughters of radionuclides that contaminate the instrumentation. This report quantifies the increasing background rates caused by cosmogenic activation in the experiment's copper instrumentation that is stationed above ground for an extended period of time. It is found that an appreciable background rate reduction can be achieved by either re-fabricating the experiment's cryostat with new, low-exposure copper (which poses several logistical issues), or by allowing a 3-year cooldown period for these pieces. Since neither of these options are practical or cost-effective, it is recommended that the experiment allow cosmogenic activation to account for up to 15% of its background budget.

This report secondarily confirms an issue with Geant4's production cuts mechanism. Secondary particles that are within the safety of a volume boundary are not expected to be removed from the stack by production cuts, but the contrary has been observed for electromagnetically neutral secondaries. Using `TestEm5` - an example application that ships with Geant4 - it is confirmed that safety is calculated correctly for all secondaries and that neutral secondaries are not cut away. The `ApplyCuts` flag is investigated given its ambiguous nature in the program's documentation. A solution to this issue for neutral secondaries is not found, but it is emphasized that this issue is of moderate importance to the SuperCDMS collaboration's simulations efforts. Further investigation of each standard electromagnetic physics list is warranted.

ACKNOWLEDGMENTS

First, I would like to thank Pekka for his unwavering support, guidance, and tenacity in pursuing academic excellence. I have taken an admittedly unorthodox path through the University of Toronto's graduate program, which you were happy to tackle alongside me. Perhaps more important than the academic training you have afforded me, is the personal growth I have seen while working with you. I am a better academic and person because of the time I have spent working with you.

I extend the same gratitude to my wonderful postdoc, Madelaine. Not only did you help me overcome an uncountable number of academic hurdles, but you were constantly there to reassure and remind me that everyone starts somewhere. This report, my academic skill set, and my character, have benefited immensely from your guidance.

To Ziqing, and Miriam, both of whom I bitterly regret not having spoke to more; your lighthearted demeanor and unrivaled level of rigor in your work have set a clear example for me to follow. You both are role-models of the highest caliber.

To Warren, who helped keep me sane as I underwent the most severe academic turmoil I have ever confronted. You are going to thrive in this program.

Finally, to my family. There's a chance you may not understand everything I've written in this report, but that won't stop you from reading it cover-to-cover. For that, I am grateful beyond what words can express.

Contents

List of Figures

List of Tables

GLOSSARY

ALP	Axion-Like Particle
BSM	Beyond the Standard Model
CP	ColdPlate
C-P	Charge-Parity
CDM	Cold Dark Matter
CDMS	Cryogenic Dark Matter Search
CDMSlite	CDMS low-ionization threshold experiment
CMB	Cosmic Microwave Background
DM	Dark Matter
DMC	Detector Monte Carlo
ER	Electronic Recoil
HV	High Voltage
iZIP	interleaved Z-Sensitive Ionization and Phonon
kky	kg $\cdot$ keV $\cdot$ year
LH	Liquid Helium
LNGS	Laboratori Nazionali del Gran Sasso
MWE	Meter Water Equivalent
MC	Mixing Chamber
NTL	Neganov-Trofimov-Luke
NR	Nuclear Recoil
QCD	Quantum Chromodynamics
ROI	Region Of Interest
SLE	Sea-Level Equivalent
SM	Standard Model
SNO	Sudbury Neutrino Observatory
SUL	Shallow Underground Laboratory
SUSY	Supersymmetry
WIMP	Weakly Interacting Massive Particle
ΛCDM	Standard Model of Cosmology

Chapter 1

INTRODUCTION

In 2012, the Standard Model (SM) of particle physics took a staggering leap forward; CERN announced that the Large Hadron Collider's ATLAS and CMS collaborations had observed a new particle, and confirmed in the following year that these signals were consistent with properties of the Higgs boson [1, 13]. This was a monumental moment in the history of physics, but also a departure from the relative comfort that the particle physics community had enjoyed for a century prior. In that time, we could predict with great precision "where" to find another elementary particle. That is, we knew which energy ranges to probe and find our next discovery thanks to resonances in scattering processes.

The Higgs boson did not afford us this luxury; its mass is a free parameter of the SM. In similar fashion, the SM provides no information on the nature of dark matter (DM). Instead, contemporary particle physics is forced to hunt for Beyond the Standard Model (BSM) particles by systematically ruling out where (e.g., mass, SM couplings, cross sections, etc.) we expect to find them.

Searches for DM are motivated by a wealth of cosmological evidence suggesting an abundance of a non-baryonic, non-luminous, and otherwise weakly interacting type of matter in the universe. Examples of these observations include galactic rotation curves [16], gravitational lensing and x-ray observations of the "Bullet" cluster [14], and myriad other phenomena [36].

On account of its weak coupling to the SM sector through the strong, weak, and electromagnetic forces, DM has yet to be detected directly. Consequently, many of its important properties such as the nature of its interactions with SM particles, mass, and small-scale structure, are unknown. Without evidence to guide DM searches in a particular direction, there exist many experiments employing different detection mechanisms that can probe a wide range of DM masses in an effort to observe it.

One of these DM searches will be the Super Cryogenic Dark Matter Search at SNOLAB (SuperCDMS SNOLAB). It is a low-energy threshold direct detection experiment that aims to search for DM particles with masses between approximately $m_\chi \sim 100$ keV and $m_\chi \sim 5$ GeV, which cause recoil energies typically in the range of 1-10 keV [35]. While these thresholds are achievable with a traditional high-purity germanium detector, CDMS-style detectors provide information on a particle's position in the crystal when it causes a recoil.

Using cryogenic silicon and germanium crystals as detectors, the experiment has excellent energy resolution and significantly reduced noise coming from thermal fluctuations in the form of phonons which are not caused by nuclear recoils. Additionally, the two-kilometer deep SNOLAB cavern that houses the detectors provides shielding from cosmic rays which otherwise would contribute to detector backgrounds.

Nonetheless, the detectors are expected to suffer from several other sources of background interactions. A prominent source are the decay daughters of radionuclides induced in copper components of the experiment by cosmic rays while they are aboveground. This process is known as cosmogenic activation.

1.1 Motivation

In DM searches, it is vital to understand the origin of background signals, the defining features of each spectrum (e.g., how a signal from an x-ray is distinct compared to a signal from a neutron), and how to separate these events from potential DM events.

To this end, SuperCDMS tracks the location history of each component in the experiment to catalog its exposure to cosmic rays. In doing so, it has become clear that the fabrication and transportation of some commercially-sourced copper components has taken longer than the 180 day sea-level equivalent (SLE) period anticipated in the experiment's technical design report. In fact, many copper pieces that comprise the cans in the experiment's cryostat (see Section 1.5.2) have seen up to 1200 days of SLE exposure.

As a result, these components garner a growing concentration of radioactive nuclides, whose decays contribute to undesirable signals observed in the detectors. In turn, cosmogenic activation occupies an increasing portion of the experiment's background budget. Therefore, it is prudent to model the background spectra produced by each component as a function of the time it has spent both above-ground and underground, which is the principal focus of this report.

The data used to generate background spectra is obtained from modelling SuperCDMS SNOLAB's geometry with the distribution of copper defined by the detector simulation SuperSim: A Geometry ANd Tracking (Geant4)-based simulations platform [5, 9, 10]. This report secondarily aims to confirm and troubleshoot a suspected issue with Geant4's (and by extension, SuperSim's) modelling of low-energy secondary particles. While such an investigation is minimally important to the present background study, it is moderately important to the collaboration's overall simulations effort since a positive outcome can reduce runtimes on CPU-intensive jobs.

1.2 Observational Evidence for Dark Matter

Myriad phenomena at different scales motivate the hypothesis and search for DM. This section will expand upon the aforementioned observational evidence of DM - such as galactic rotation curves and gravitational lensing. Subsequent sections will detail particle candidates for DM which are relevant to SuperCDMS and the important features of direct detection experiments.

1.2.1 Galaxies

Galaxies are systems of gravitationally-bound stars and gas which possess luminous and non-luminous components. Broadly speaking, the luminous large-scale structure of a spiral galaxy (the subject of study for this section) is composed of a central bulge where the mass density of the galaxy is highest, a thin stellar disc which extends beyond the central bulge, atomic gas composed primarily of hydrogen which extends even further than the stellar disc, warm ionized gas, and molecular gas [16].

Based on observations of the luminous mass in a spiral galaxy, one would expect the linear velocity of a mass in its disc to obey the following relation:

$$v(R) = \sqrt{\frac{GM(R)}{R}}, \tag{1.1}$$

where $G = 6.67 \times 10^{-11}$ N·m$^2 \cdot$ kg^{-2} is the universal gravitational constant and $M(R)$ is the mass contained in a sphere of radius R.

Equation 1.1 is inconsistent with optical measurements of the spiral galaxy M31 (i.e., Andromeda) initially taken by Ford and Rubin in 1970 [29]. The same authors later corroborated this result with measurements of 21 spiral galaxies in 1980 [28]. By observing different emission regions of M31 at distances between 3-24 kpc from its nucleus, ref. [29] found that the galaxy's velocity dependence as a function of radius is mostly flat well beyond its central bulge. A correlation of this nature suggests that a large fraction of the galaxy is composed of non-luminous matter extending to large galactocentric distances.

The behaviour typical of these measurements is shown in Figure 1.1, which does not have the form $v \propto R^{-1/2}$. The measurements of spiral galaxy M33 instead display a mostly flat correlation which is observed above 3 times the galaxy's scalelength (the distance from a galaxy's centre at which its brightness decreases by a factor of e) of

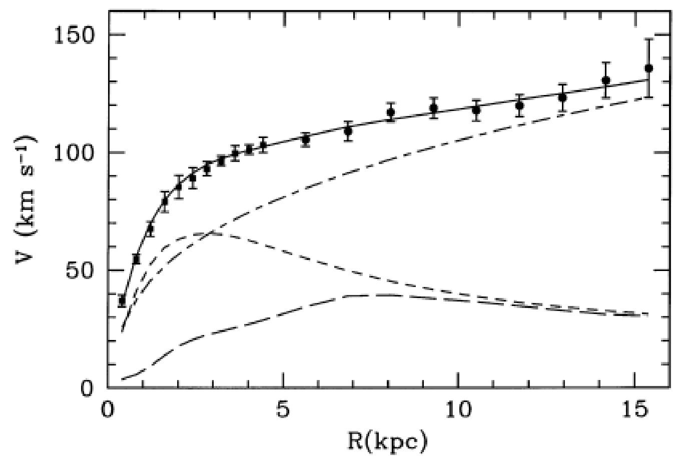

Figure 1.1: Rotation curve (points) of the spiral galaxy Messier 33 obtained through measurements of its 21-cm hydrogen emission line. Also included are the best fit model (solid line), DM halo contribution (dot-dashed line), the stellar disc (short-dashed line), and the gas contribution (long-dashed line). Image taken from ref. [16].

$R_d = 1.2$ kpc [16]. Indeed, it was concluded therein that the galaxy's gravitational potential comes primarily from dark mass extending up to 14 disc scalelengths.

1.2.2 Galaxy Clusters

Galaxy clusters are massive objects composed of galaxies and intergalactic gas. The latter is accelerated by gravity to produce measurable x-ray signals through thermal bremsstrahlung emissions.

Galaxy cluster mergers provide unique opportunities to detect non-luminous mass via gravitational lensing effects. Einstein's general relativity tells us that light will follow geodesics in a curved spacetime caused by the gravitational potential of an object. If a sufficiently massive object exists between a background source and an observer, light from the source will become measurably distorted proportional to the object's mass before reaching the observer. The results is multiple images, or a single distorted image depending on certain conditions.

In *strong* gravitational lensing, the source object is nearly behind the lens and light travelling along several paths is deflected towards an observer. In this case, multiple images or a so-called “Einstein ring” can be observed, and the object appears more luminous. In contrast, *weak* gravitational lensing has less favourable geometry which results in a sheared image, causing distant objects to appear more elliptical than they otherwise would. Zwicky used the principle of strong lensing to suggest that galaxy clusters possess more than just their observed luminous mass. Specifically, he had made observations of the velocities of galaxies in the Coma cluster which disagreed with the accepted value (based on observations of luminous matter) by a factor of 400, and put forth the idea of gravitational lensing as a technique for determining galactic masses [37].

A useful contemporary example of using weak lensing to observe dark matter is the “Bullet” cluster merger. The merger is composed of a less massive Western subcluster and a doubly massive Eastern cluster, both of which have moved ahead of their respective x-ray emitting plasma clouds due to drag caused by collisions during the merger. This gives rise to the characteristic shape of a bow shockwave, hence the name “Bullet” cluster.

These conditions provide two distinct, luminous sources of gravitational potential that can be used to verify if additional non-luminous matter is present in the merger: The aforementioned plasma cloud, and the baryonic matter in each galaxy cluster.

Ref. [14] postulates the following: In the absence of DM, the primary source of gravitational potential based on weak lensing observations originates from the plasma cloud since baryonic matter will have slowed down through collisions during the merger. Conversely, if collisionless DM is present, then it is expected to be spatially coincident with both clusters rather than the intracluster gas (which comprises the bulk of the merger’s visible matter). In this case, the potential would trace the mass of the east and west clusters. Weak lensing observations showed that the majority of matter in the merger is east and west of the visible cluster, suggesting that DM comprises the bulk the merger.

1.2.3 Cosmic Microwave Background

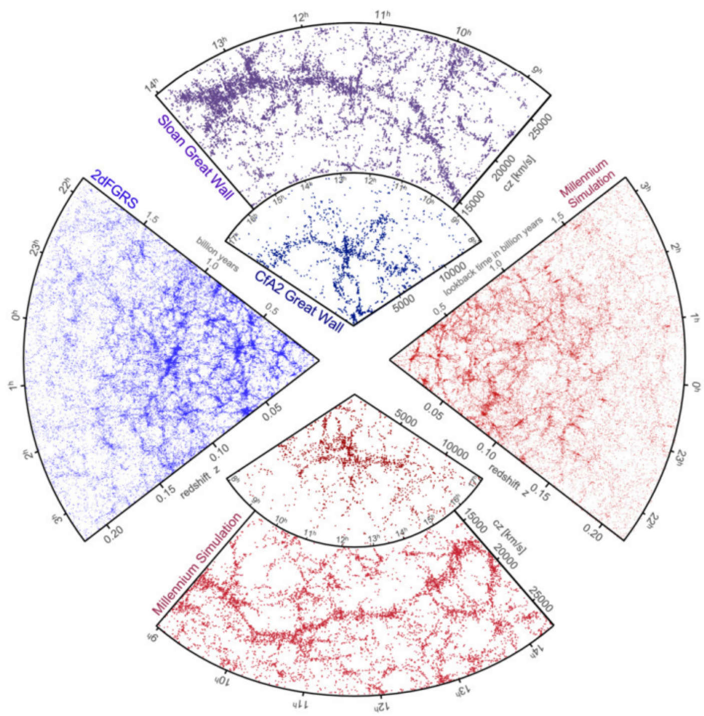

Figure 1.2: Simulated and observed distribution of large scale structure in the universe with Millenium simulation in red and observational maps in blue. Image taken from [11].

After the Big Bang, the universe consisted of a hot, dense, opaque plasma of elementary particles. In this fully ionized universe, photons interacted primarily with electrons through Thomson scattering and their mean free path was relatively small. Therefore, any hydrogen atoms formed through radiative recombination would be photionized shortly thereafter. For perspective, according to the Standard Model of Cosmology (ΛCDM), the scattering rate of a photon in a 70 year-old universe would have been approximately three events every week [30]. In contrast, the rate today (crudely assuming the same ion number density) would be once every $\sim 1.4 \times 10^{13}$

years!

The strong coupling between photons and electrons lasted until the rate of expansion of the universe exceeded the scattering rate of photons off of ions. Thereafter, the universe cooled sufficiently to allow free electrons to combine with free protons; forming hydrogen atoms and ejecting photons. These decoupled photons, along with those which were already present in the plasma "bath" when their mean free paths were minuscule, are what we observe as the CMB today.

After recombination and photon decoupling, atoms experienced gravitational attraction and formed increasingly larger structures. This process begun with minute density perturbations, which eventually gave way to the large scale structures such as galaxies that we observe today. To model this evolution, the Millenium Simulation considered DM as collisionless (i.e., weakly self-interacting) to distinguish it from baryonic matter and recovered excellent agreement with observational maps of large scale structure in the CMB taken by CfA2, 2dFGRS, and SDSS [11]. Figure 1.2 illustrates the Millenium map alongside the observational maps, with each point indicating the presence of a large luminous structure such as a galaxy or cluster.

The excellent agreement between these maps provides compelling evidence for DM at cosmological scales. With this, an argument for the existence of DM on several scales has been established. Next, a discussion of its nature is in order.

1.3 Dark Matter Candidates

Only some macroscopic properties of DM are known. For instance, it is stable over cosmological time scales, interacts relatively strongly through gravity, is likely collisionless, and cold (i.e., non-relativistic) [11].

The particle nature of DM, however, is subject to scrutiny by numerous experiments. This section will explore particle candidates for DM that are of interest to the SuperCDMS SNOLAB experiment.

1.3.1 Weakly Interacting Massive Particles (WIMPs)

A well-motivated candidate for particle DM is the WIMP; a somewhat ambiguous term which generally refers to a type of massive, non baryonic, cold dark matter (CDM) which interacts through channels that are lower in energy than the weak scale. CDM simply means that DM particles are non-relativistic.

More recently, the term "WIMP" has come to refer to particles in the mass range 10 GeV - 100 TeV whose interactions with SM particles are strongly suppressed in order to avoid conflicts with known upper bounds on cross section measurements [18].

WIMPs are a favoured candidate for DM because they produce the relic abundance observed today through thermal freeze out; the so-called WIMP Miracle. In this regime, DM and SM particles are in thermal equilibrium while the early universe has a temperature larger than the DM particles' mass. However, cooling and expansion of the universe results in DM particle production becoming kinematically forbidden while also making them too dilute to self-annihilate. Therefore, thermal freeze-out causes the abundance of DM relics to asymptotically approach their constant relic density according to the Boltzmann equation:

$$\frac{dn}{dt} = -3Hn - \langle \sigma_A v \rangle (n^2 - n_{\text{eq}}^2), \tag{1.2}$$

where n is the number density of a particular DM particle, H is the Hubble parameter, $\langle \sigma_A v \rangle$ is the thermally averaged annihilation cross section, and n_{eq} is the equilibrium number density of the DM particle in thermal equilibrium. A more thorough treatment of thermal freeze out is found in [18]. By this criterion, it is then also reasonable to generalize "WIMP" to mean any DM particle which produces the expected thermal relic abundance.

A popular model-specific example of a WIMP is the neutralino. These hypothetical particles are combinations of superpartners of the photon, Z boson, and Higgs boson which rose to popularity as a solution to the gauge hierarchy problem in the 1980's. Neutralinos are described by a proposed extension to the SM called Supersymmetry (SUSY), where each SM particle has a corresponding superpartner with identical quantum numbers and gauge interactions but with a different spin. Specifically, the *lightest* neutralino is a promising WIMP candidate given its mass range (2 GeV - 10^4 GeV) and its wide variety of interaction cross sections. Reference [27] provides a more detailed explanation on the neutralino as well as several other WIMP candidates.

While SUSY has captivated the attention of many WIMP searches in past years, there is no evidence in favour of the theory from CERN's Large Hadron Collider. As a result, experiments such as SuperCDMS have been searching for low-mass (≤ 10 GeV) DM particles in accordance with emerging theories such as asymmetric DM and dark sectors [3]. One such proposed particle was initially put forward as a solution to the strong CP problem of quantum chromodynamics (QCD) in 1977 by Peccei and Quinn: The axion.

1.3.2 Axions

For decades, it has been well-known that the weak force does not respect charge-parity (CP) symmetry through various measurements of neutral kaon [19] and B meson [2] systems.

The strong force, in principle, similarly permits C-P violation through a term in the QCD Lagrangian proportional to $g_s^2 \theta G^{\alpha}_{\mu\nu} G^{\alpha}_{\rho\sigma}$, where g_s is the strong coupling, θ is a free phase parameter, and $G_{\mu\nu}$ is the gluon field strength tensor. However, limits on the neutron electric dipole moment suggest that θ is exceedingly small ($\theta \sim 10^{-10}$);

a fine-tuning problem. This motivates the introduction of a new pseudoscalar field, dubbed the axion. The particle's precise theoretical motivation is explored in ref. [18].

Axions are predicted to have a mass in the range of 6 μeV - 6 meV, determined perturbatively to be inversely proportional to the axion decay constant f_a:

$$m_a = \frac{\sqrt{m_u m_d}}{m_u + m_d} m_\pi f_\pi \frac{1}{f_a}, \tag{1.3}$$

where m_u, m_d and m_π are the masses of the SM up quark, down quark, and pion, respectively, and f_π is the pion decay constant. Cosmological observations and the requirement that the axion relic density must be less than or equal to the total observed DM relic density constrain the decay constant to the range 10^9 GeV $\leq 10^{12}\theta_i^2$ [18]. The angle θ_i is the vacuum misalignment angle determined by the value of the axion field prior to spontaneous breaking of its U(1) symmetry at an energy scale f_a in the early universe, and assumes a non-thermal production mechanism. Additionally, axions are feebly interacting with themselves, photons, and fermions given that each coupling is suppressed by the symmetry breaking scale f_a [22].

Finally, it is important to note that if we assume axions are produced thermally, they will occupy a minuscule fraction of the total relic density, rendering non-thermal axions a more tantalizing DM candidate.

One of SuperCDMS SNOLAB's science goals is to probe the electron couplings of 1-100 eV axions and Axion-Like Particles (ALPs) [7]. The latter refers to an axion which is not required to solve the strong C-P problem; it does not warrant further discussion in this report.

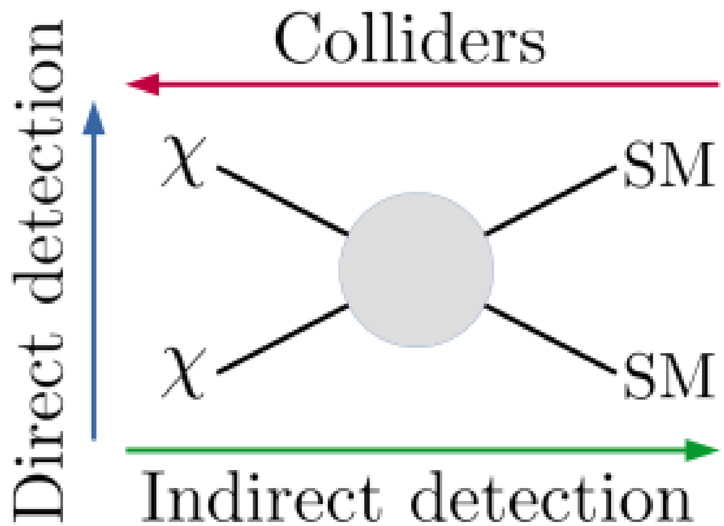

Figure 1.3: Schematic representation of different dark matter detection channels [11]. Direct detection relies on some detectable elastic nucleonic interaction between a DM and SM particle. Indirection detection aims to observe products of DM interaction such as gammas originating from DM-DM annihilation. Collider searches attempt to infer DM signals through missing energy in SM-SM events.

1.4 Direct Detection of Dark Matter

There are three main categories of DM detection: direct detection, indirect detection, and accelerator searches. These detection channels are represented schematically in Figure 1.3. SuperCDMS utilizes cryogenic semiconducting silicon and germanium crystals as detector volumes, making it a is a direct detection experiment. Therefore, this will be the detection category that will be the focus of this work.

Direct detection experiments rely on sensitive detectors and low backgrounds to detect minute nuclear recoils (NRs) and electron recoils (ERs) caused by interactions of DM with SM particles. The distinction between an NR and an ER is vital: The former originates from nucleon-coupled DM, neutrons, and coherent elastic neutrino-nucleus scattering (CEνNS) while the latter originates from backgrounds which interact via the electromagnetic force. NRs are detected primarily as phonon signals with limited charge signals due to the detectors' ionization yields, whereas ERs can be observed via scintillation or ionization signals. For SuperCDMS SNOLAB, both ERs and NRs be observed through either phonon or ionization signals. The mechanism behind this will be explained in Section 1.5.1.

There are several barriers to WIMP detection. First, assuming a Maxwell-Boltzmann velocity distribution with root-mean-square velocity $\sim$ 220 km/s (equivalently, 7.5×10^{-4} c) for WIMPs, we can find the maximum energy transfer to a nucleus in a $\chi + N \to \chi + N$ elastic scattering event. Crudely assuming that the WIMP and nucleus masses are both $m_\chi = m_N = 50$ GeV,

$$\begin{aligned} T_{\max} &= \frac{4m_\chi m_N}{(m_\chi + m_N)^2} T_\chi \\ &\sim \frac{4 \times 250\ \text{GeV}^2}{(100\ \text{GeV})^2} \times \frac{1}{2} \times 50\ \text{GeV} \times (7.5 \times 10^{-4} c)^2 \\ &= 1.41\ \text{keV}. \end{aligned}$$

So it is clear for a WIMP even with a mass near that of the weak gauge bosons, only a relatively small NR can be observed.

Second, we can calculate the expected rate of WIMP scatters using the following:

$$\frac{dR}{dE_R} = \frac{\rho_0 M}{m_N m_\chi} \int_{v_{\min}}^{v_{\max}} v f(v) \frac{d\sigma}{dv} dv \tag{1.4}$$

$$\propto \exp\left(-\frac{E_R}{E_0} \frac{4m_\chi m_N}{(m_\chi + m_N)^2} \right) \tag{1.5}$$

where E_R is the NR energy, $\rho_0 = 0.3$ GeV/cm^3 is the local DM density, $f(v)$ is the aforementioned WIMP velocity distribution, E_0 is the WIMP's most probable kinetic energy, and M is the target mass of the detector. The minimum WIMP velocity is determined by the sensitivity of the experiment's detector and the maximum velocity is simply the escape velocity of the Milky Way galaxy. The latter can equally be taken to infinity, since WIMPs that have escaped the galaxy will not be observed

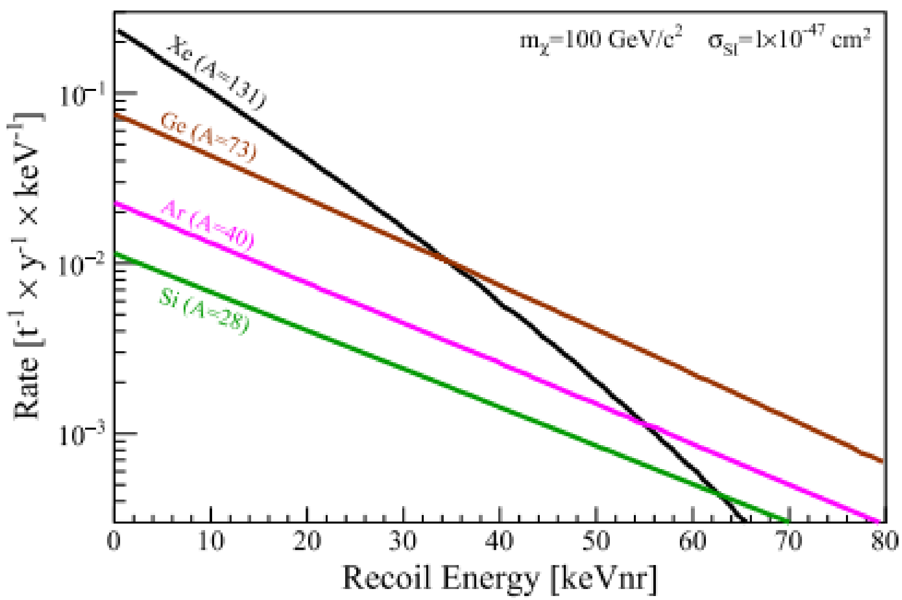

Figure 1.4: Nuclear recoil spectra caused by a 100 GeV WIMP in different target materials assuming a spin-independent cross section $\sigma_{\rm SI} = 10^{-47}$. Image taken from [32].

[32].

Integrating equation 1.4 and multiplying it by an observing time T,

$$N = T \int_{E_{\rm low}}^{E_{\rm high}} \epsilon(E_R) \frac{dR}{dE_R} dE_R, \tag{1.6}$$

where N is the number of scattering events, $E_{\rm low}$ is the detector energy threshold, $E_{\rm high}$ is the energy of a WIMP moving at the Milky Way's escape velocity, and ϵ is the detector efficiency. The area under Figure 1.4 gives an idea for the magnitude of this quantity. Reference [15] (which, coincidentally, was written by the current executive director of SNOLAB!) gives an in-depth derivation for each of these equations.

It is important to note that the velocity distribution is subject to change. While the DM halo moves at a local speed of $\langle v \rangle = 220$ km/s, the Earth and the sun are also moving through it. Compounding these velocities results in an annual modulation of the DM flux through direct detection experiments, causing a harder WIMP spectrum in the summer and a softer WIMP spectrum in the winter [32].

The SuperCDMS collaboration has also performed analyses to probe inelastic channels, namely bremsstrahlung emissions and the Migdal effect. These interaction regimes have recently become popular in the search for signals of sub-GeV mass DM [8].

1.5 SuperCDMS SNOLAB

SuperCDMS SNOLAB will be located 2 km undergound in Vale's Creighton Mine near Sudbury, Ontario. It is the successor to SuperCDMS Soudan, which was located in Minnesota's Soudan Mine, under 700 m of rock overburden. This study will put special emphasis on sources of background and the cryostat. Interested readers are encouraged to consult ref. [7] for a detailed report on the upgrades, expected science reach, and instrumentation of the experiment.

1.5.1 Detectors

The SuperCDMS SNOLAB experiment will house four detector towers connected to a dilution refrigerator, each containing six detectors cooled to $\sim 15 - 30$ mk. The detectors consist of cryogenic silicon and germanium crystals. Two detector designs with similar physical dimensions (10 cm across by 3.3 cm tall) will be deployed: interleaved Z-Sensitive Ionization and Phonon (iZIP) detectors, and High Voltage (HV) detectors.

iZIP detectors use ionization yield models to discriminate between ERs and NRs, affording them better sensitivity than HV detectors above dark matter particle masses $m_\chi \sim 5$ GeV. They employ a small bias voltage ($\pm$ 3 V for Ge and $\pm$4 V for Si) on the top and bottom ionization electrodes to generate a vertical electric field and collect drifting charges.

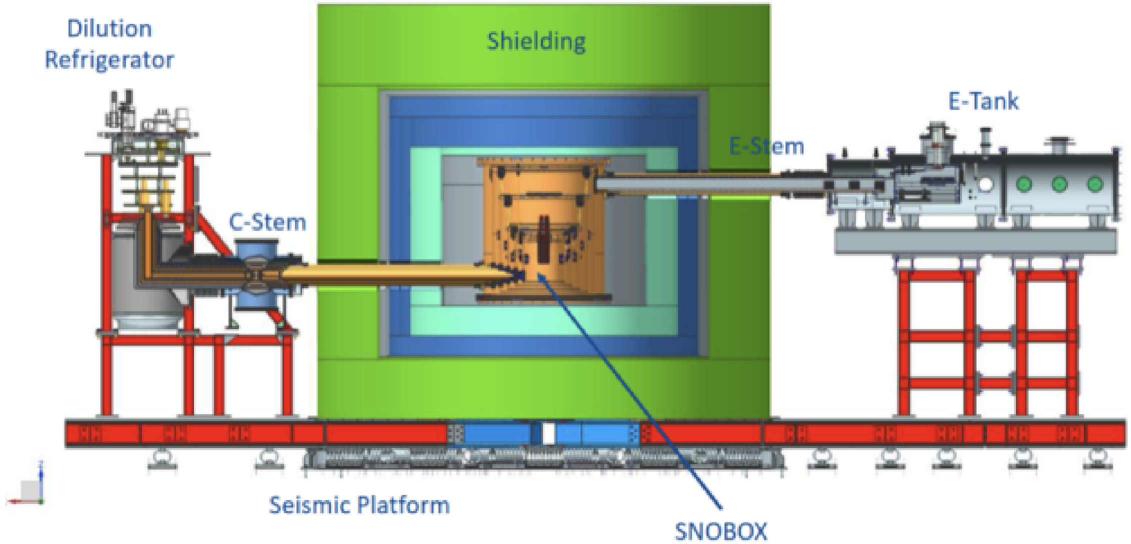

Figure 1.5: Schematic of the SuperCDMS SNOLAB experiment resting on its seismic platform. The passive shield consists of a water tank, polyethylene, and lead - all of which house a cryostat (SNOBOX) containing six nested copper cans corresponding to different thermal stages. A Cold-Stem and an Electronics-Stem connect the detectors to a commercial dilution refrigerator and the electronics tank, respectively. Image taken from [7].

Conversely, HV detectors do not discriminate between ERs and NRs on an event-by-event basis. Instead, they employ a 100 V bias voltage and exploit the Neganov-Trofimov-Luke (NTL) effect [23] to amplify phonon signals proportional to the amount of work performed on drifting charges by the electric field. NTL phonon amplification affords HV detectors a significantly reduced recoil-energy threshold, making them more sensitive to the $m_\chi < 5$ GeV region.

Table 1.1 contains the total number of detectors, total exposure and resolutions for each, and their voltage biases. Exposures are based on four years of operation with an 80% live time. Note the units of exposure are in units of kg·yr, where the mass component is derived from the target (i.e., detector crystal) mass [7].

Table 1.1: The anticipated exposures and detector parameters for the SuperCDMS SNOLAB experiment [3]. Ionization resolutions are slightly different in Ge and Si due to their minutely different band gaps.

	iZIP		HV	
	Ge	Si	Ge	Si
Number of detectors	10	2	8	4
Individual mass (kg)	1.39	0.608	1.39	0.608
Total exposure (kg·yr)	56	4.8	44	9.6
Phonon resolution (eV)	50	25	10	5
Ionization resolution (eV)	100	110	-	-
Voltage bias (V)	6	8	100	100
Region of Interest (keV)	[1, 50]	[1, 50]	[0.003, 2]	[0.003, 2]

1.5.2 Cryostat and Shielding

The cryostat - also referred to as the SNOBOX - consists of six nested copper cans suspended by kevlar ropes, surrounded by a layer of polyethylene to shield the internals from radiogenic and cavern neutrons. In turn, the polyethylene is surrounded by a 23-cm thick layer of lead to shield from gamma rays. The next layer outward is a thin segment of aluminum that will protect the detectors from radon daughters. From this layer inwards, the shield will be purged with nitrogen gas to reduce Rn levels. Finally, the outermost layers of shielding will consist of another layer of polyethylene and a water tank. In addition, a mu-metal shield will rest inside all of the layers of shielding but outside of the cryostat to reduce the effects of Earth's magnetic field on the detectors.

Each copper can corresponds to a different thermal stage that is colder than the one surrounding it to sink dissipated thermal power. The outermost can, the Outer Vacuum Chamber (OVC), resides at ambient temperature and accommodates the cryostat's insulating vacuum. The subsequent layers, listed in order of the outermost can to the innermost can, are the copper shield (SH), liquid helium (LH), still (ST), cold plate (CP), and mixing chamber (MC). These stages are expected to be kept at

50 K, 4.5 K, 1 K, 250 mK, and 15 mK, respectively.

Each tower is mounted to the MC while also thermally coupled to the four inner cans. Of the four cans it is connected to, it is heat sunk to the lid of the inner three. The cryostat is penetrated on one side by the Electronics Stem (E-Stem), which carries signal cables and cooling fluid lines transporting gaseous or liquid helium from the Electronics-Tank (E-Tank). On the other side, the Cold-Stem (C-Stem) connects a dilution refrigerator to the cans.

The entire assembly rests on a seismic platform intended to attenuate movement induced by geological activity.

1.6 Background Sources

The SuperCDMS SNOLAB experiment will be subject to several sources of background. Broadly speaking, there are seven categories of background sources in consideration [3]:

1. Detector contamination, such as naturally occurring, long-lived ^{32}Si in the detector crystals, cosmogenically-induced tritium, and Ge activation lines originating from cosmogenic isotopes in detector crystals decaying via electron capture,

2. Material activation resulting from exposure to high-energy cosmic rays and producing long-lived radionuclides in a material. This is discussed at length in Section 2.1,

3. Material contamination, wherein radioactive impurities with long decay chains such as ^{232}Th and ^{238}U are implanted into a component during manufacturing. Additionally, naturally ubiquitous and long-lived isotopes such as ^{40}K and ^{60}Co produce background signals,

4. Surface contamination, such as airborne dust containing radionuclides whose daughters can plate out onto important components such as detector housings. These daughters can furthermore induce long-lived radioactive isotopes such as ^{210}Pb in the apparatus. Contaminated surfaces with and without line of sight to the detectors are both problematic; the former is concerning because there is no shielding between the implanted contaminant and the detector. The latter is concerning because background sources such as x-rays (in the form of decay daughters and bremsstrahlung photons from betas), gammas, and neutrons are capable of reaching the detectors,

5. Cavern gamma rays, neutrons or radon (the latter of which is abundant in air in Creighton Mine, necessitating a low-radon clean room to assemble detector components, and nitrogen purging of the detector located on the seismic platform),

6. Cosmic ray induced backgrounds in the cavern such as neutrons produced via spallation of cosmic ray muons. This is also discussed in Section 2.1. Finally,

7. Coherent Elastic Neutrino-Nucleus Scattering (CEνNS) from solar neutrinos, which is not expected to be problematic at the experiment's outset, but will become a significant source of background as the sensitivity of DM detectors come closer to the cross section for this background.

1.6.1 Normalized Bacgkround Rate and Analysis Cuts

In order to better understand how each source of background will contribute to signals observed in the detectors, Monte Carlo simulations are performed using the SuperCDMS SNOLAB geometry in SuperSim (see Section 3.1). Background rates must be normalized prior to comparison to account for factors such as the radioactivity of an isotope, target mass, and the number of simulated primaries.

Therefore, the background rate for an energy Region Of Interest (ROI) is normalized according to:

$$R_{\mathrm{ROI}}\left[\frac{\mathrm{counts}}{\mathrm{kg}\cdot\mathrm{keV}\cdot\mathrm{y}}\right] = C\left[\frac{\mathrm{counts}}{\mathrm{primary}}\right] \times \frac{1}{M_{\mathrm{ROI}}\Delta E_{\mathrm{ROI}}[\mathrm{kg}\cdot\mathrm{keV}]} \times R_i\left[\frac{\mathrm{decays}}{\mathrm{year}}\right] \times F_p\left[\frac{\mathrm{primaries}}{\mathrm{decay}}\right], \tag{1.7}$$

where R_{ROI} is the normalized rate in the energy region of interest, C is the fraction of simulated events that generate an event in the ROI, M and E are the target mass and energy for the ROI, R_d is the decay rate of a particular contaminant, and F_p is the average primary production rate per decay. For this investigation, $F_p = 1$ since SuperSim permits direct simulation of decays of interest using Geant4's radioactive decay module.

It is also common to use units of counts $\cdot$ kg^{-1} $\cdot$ keV^{-1} $\cdot$ d^{-1}, often referred to as differential rate units (dru) in background studies. However, this report will use those presented in equation 1.7 for background rates with the abbreviation kky^{-1}.

SuperSim produces data files with a minimal set of cuts to retrieve raw rates from each detector with the assumption that analysis cuts will be applied at a later time. There are several categories of analysis cuts that are relevant to this investigation: singles vs. multiples, bulk vs. surface events, and particle types.

It is unlikely that a WIMP will scatter multiple times, meaning that events which produce signals in more than one detector are more likely from background events. Any event which produces more than a single hit above 350(175) eV in a Ge(Si) iZIP detector, or 70(35) eV in a Ge(Si) HV detector, within 1 ms from the initial energy deposition is counted as a multiple and subject to analysis cuts [3]. ER *singles* will therefore be examined, since they are expected to cause the most significant *background* spectra.

Next, both iZIP and HV detectors are able to reject surface backgrounds to some degree. Therefore, it is more interesting to examine the backgrounds induced in a detector's *bulk*, i.e., more than 100 μm from its surface to better understand how to subtract them from observed spectra. These backgrounds are classified as *bulk* event sources.

With these analysis criteria, the event types of interest for this report are *bulk ER singles*.

Chapter 2

Cosmogenic Activation in Copper Components

2.1 Cosmogenic Activation as a Source of Background

The activity of a material is defined by its rate of decays:

$$A_i(t) = -\frac{dN_i}{dt}, \tag{2.1}$$

where $A_i(t)$ is the activity as a function of time, and N_i is the number of radioactive atoms present in the material. From this, it is possible to derive a formula for the activity induced in a sample after an *exposure time*, t_{exp}:

$$N_i(t_{\text{exp}}) = \tau_i R_i (1 - e^{-\tau_i t_{\text{exp}}}), \tag{2.2}$$

where τ_i is the activated nuclide's lifetime and R_i is its rate of production. The latter is given by:

$$R_i = \sum_j N_j \int \sigma_{ij}(E)\phi(E)dE, \tag{2.3}$$

where N_j is the number of target atoms, σ_{ij} is the production cross section of a particular isotope i within a target j (occasionally referred to in the literature as the *excitation function*), and ϕ is the flux of cosmic rays (primarily neutrons and a limited contribution from protons). In some cases, there exist direct measurements of this parameter, but they are resource-intensive to obtain and therefore not generally available. Accordingly, production rates of different isotopes are typically calculated using the flux of cosmic rays and their production cross sections using 2.3. Production cross sections can be obtained from computational tools such as TALYS [12, 25].

Also note the distinction between N in equation 2.1 and N_j in equation 2.3: The former refers to the number of contaminant atoms produced (e.g., how many ^{60}Co atoms are induced in a pure copper sample) and the latter refers to the number of atoms in a target material (e.g., how many atoms are present in the copper sample). The subscripts above will henceforth be dropped with the understanding that the production rates, decay constants, and number of atoms are specific to a cosmogenic isotope.

Additionally, each component of the experiment will not observe a constant rate of exposure; various pieces spend time in environments which provide higher levels of screening to cosmic rays, such as SNOLAB or the Pacific Northwest National Laboratory's Shallow Underground Lab (SUL). It is noted in [12] that an overburden depth of a few tens of meters of water equivalent would be sufficient to reduce the proton and neutron component of cosmic flux to negligible levels. Given that SNOLAB boasts an overburden equivalent to 6010 meters of water [3], we can confidently take $R \to 0$ once a component enters the SuperCDMS cavern.

Reference [24] exploited measured data of neutron production rates for various slant-depths, as well as FLUKA simulations based on measured quantities such as total muon flux to parameterize the neutron flux for several laboratories, including SNOLAB. It was found that the differential flux of 1 GeV neutrons (a relevant energy for activation processes) in SNOLAB is of the order 10^{-17} cm^{-2}s^{-1}MeV^{-1}, which is significantly lower than the differential flux at sea level reported in [12] of approximately 10^{-7} cm^{-2}s^{-1}MeV^{-1}.

It should be emphasized that while the proton and neutron component of cosmic ray flux is negligible at these depths, nucleonic backgrounds originating from spallation by high-energy cosmic ray muons are still present. The spectrum of muon-induced neutron flux at these depths can extend up to a few GeV [24], but it tends to be dominated by the region of a few MeV - which is below the production threshold for activation occurring via spallation [12]. This suggests that neutrons themselves will be a more prominent source of background once components are underground rather than the relatively rare radionuclides they induce.

Furthermore, available experimental data on cosmogenically-induced nucleon flux at these depths is scarce, rendering any validation of simulated data difficult. A recent study conducted by the SNO collaboration suggests that Geant4, the foundation of the simulation platform used for this investigation, does not adequately model neutron transport in the high-energy regime ($>$ 15 MeV) based on measurements such as the lateral capture distance of follower neutrons in heavy water [6]. This is problematic for SuperCDMS, as the collaboration relies on SuperSim, which is a Geant4-based package (see Section 3.1), and data from [24] to understand background sources coming from cavern flux [7].

While a study on cosmogenically-induced cavern neutrons is beyond the scope of this report, it is nonetheless relevant to the present discussion and requires further investigation to fully understand how cosmic rays contribute to sources of background at SNOLAB.

In order to account for a sample's reduction in activity following its arrival underground and subsequent reduction of radionuclide production via cosmogenic activation, an additional decaying exponential factor is included:

$$N(t) = \tau R(1 - e^{-\frac{t_{\mathrm{exp}}}{\tau}})e^{-\frac{t_{\mathrm{cool}}}{\tau}}, \tag{2.4}$$

where t_{cool} refers to a sample's *cooldown time*. From this, we can immediately recover the formula for activity:

$$A(t) = R\left(1 - e^{-\frac{t_{\text{exp}}}{\tau}}\right)e^{-\frac{t_{\text{cool}}}{\tau}}. \tag{2.5}$$

Finally, the average activity of a cosmogenic isotope over some period of time t_{run} is,

$$A_{\text{avg}}(t_{\text{exp}}, t_{\text{cool}}, t_{\text{run}}) = \frac{\tau R}{t_{\text{run}}}\left[1 - e^{-\frac{t_{\text{exp}}}{\tau}}\right] \times \left[e^{-\frac{t_{\text{cool}}}{\tau}} - e^{-\frac{t_{\text{cool}}+t_{\text{run}}}{\tau}}\right] \tag{2.6}$$

Equations 2.5 and 2.6 are used to find the activity, and by extension, expected number of events originating from cosmogenic isotopes induced in the experiment. The former is used in equation 1.7 to normalize background rates coming from simulations, while the latter is useful in determining the number of events to feed into SuperSim and generate these rates. For a detailed derivation of the above formulae, consult Appendix A.

Measured values for the production rate of long-lived cosmogenic isotopes in natural copper are taken from [12] and tabulated below. Short-lived (i.e., less than ∼100 days) isotopes are not relevant to this background study due to the relatively long cooldown time that components in the experiment enjoy once they reach the SNOLAB cavern.

A notable exclusion from Table 2.1 is the rate of production of tritium (^{3}H) in natural copper. This long-lived ($t_{1/2} = 12.312$ y) isotope is a ubiquitous background source in many rare event searches since it is a spallation product - meaning it can be generated in any material [7, 17]. In addition, tritium exclusively undergoes beta decay. As a result, it is difficult to characterize its activation rate through experimental and computational channels. The former, because its decay products cannot easily be told apart from other sources of background; the latter, because tritium may be

Table 2.1: Measured rates of production of isotopes induced in natural copper at sea level via cosmogenic activation, their half-lives, gamma emission energies, and gamma emission probabilities. Production rates and half-lives are used to determine activities for this background study [12]. Production rates were measured at the Laboratori Nazionali del Gran Sasso (LNGS). Gamma emission energies and probabilities are taken from [17].

Isotope	Production Rate ($kg^{-1} \cdot d^{-1}$)	Half-Life (d)	Gamma Emissions (keV)	Probability (%)
^{56}Co	19.9 ± 2.6	77.24	846.8, 1238.3	100, 67.6
^{57}Co	155 ± 35	271.82	122.1	85.6
^{58}Co	142.6 ± 7.8	70.85	810.8	99
^{60}Co	181 ± 16	1923.95	1173.2, 1332.5	99.97, 99.99
^{54}Mn	18.6 ± 1.8	312.19	834.8	99.98
^{59}Fe	39 ± 10	44.49	1099.3, 1291.6	56.5, 43.2
^{46}Sc	4.6 ±1.6	83.79	889.3, 1120.5	99.98, 99.98

produced through several different reaction channels [12].

Furthermore, tritium is expected to be the dominant source of background in SuperCDMS SNOLAB germanium high-voltage (HV) detectors, with a sea-level activation rate of 74 ± 9 atoms $\cdot$ $kg^{-1} \cdot d^{-1}$ obtained through measurements taken by CDMSlite [4]. However, the activation rate of tritium in natural copper is not well-understood. In order to calculate the rate, a similar approach to [4] must be employed. Namely, one would need to adopt a neutron flux parameterization (results presented by Gordon et. al. in [20] are frequently used in the literature) and use computational tools to calculate an excitation function. Unfortunately, any results would be difficult to validate without measurements of the corresponding rate, and so tritium activation will not be considered in the background spectra presented in this report.

An extension of the work reported here is to study the background induced by tritium beta emissions in copper components of the experiment. Namely, the detector housings would be the only components of interest, since any other beta characteristic of tritium decay would be screened by the housings. Although, tritium can be straightforwardly purged from copper prior to its installation in the experiment; any such investigation should be conducted with this in mind.

Additionally, estimates on the production rate of each radioisotope, including tritium, would be improved using location and time-specific neutron flux parameterizations rather than the one given in ref. [20]. Resources such as EXPACS [31] can be used to calculate "correction factors", similarly to ref. [12], in order to better understand how production rates vary as the experiment's instrumentation is transported to its final destination.

2.2 Exposure, Cooldown, and Runtimes for Copper Components

This investigation endeavours to quantify the extent to which different exposure, cooldown, and runtime (i.e., the time taken to assemble the experiment and take data) combinations influence backgrounds. To this end, it would be helpful to first understand how these combinations affect the activity of each radioisotope in the experiment. Figure 2.1 uses equation 2.6 to illustrate how the activity varies in different scenarios.

Notice that the contour plot for ^{60}Co presents a broader range of cooldown and runtime values where the activity remains relatively high compared to every other plot. This illustrates why long-lived isotopes (see Table 2.1) are especially problematic as sources of background. For example, given an exposure and runtime of 4 years (1461 days), one would need to allow a copper sample contaminated with ^{60}Co to cool down for up to 5 years to observe a comparable average level of activity to that of a sample contaminated with ^{57}Co which had cooled down for $\sim$100 days.

The same challenge arises for tritium, which has a significantly larger half-life than ^{60}Co. To demonstrate the magnitude of its background impact, a contour plot for tritium is also included with an activation rate of 1 atom per kilogram per day.

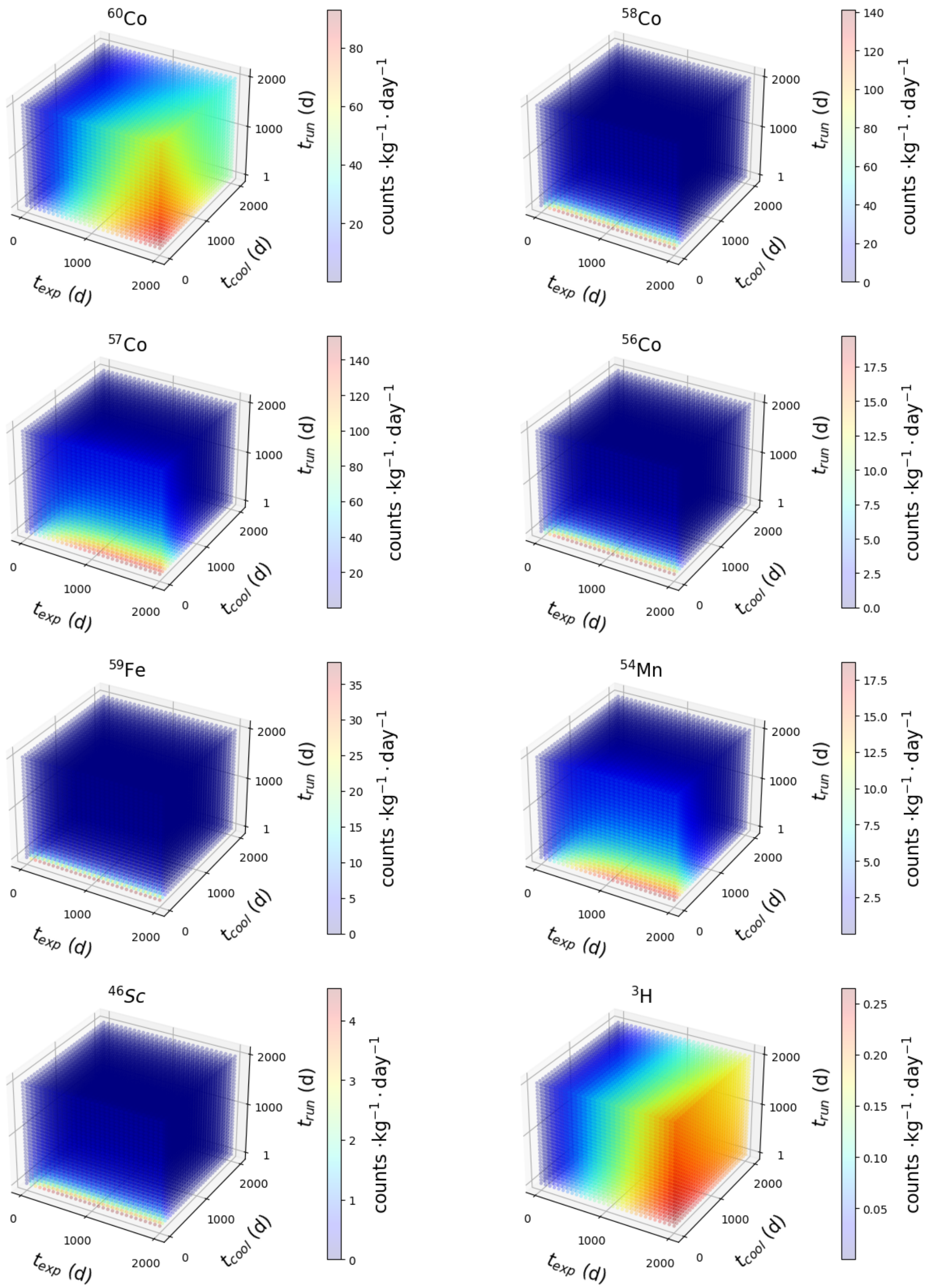

Figure 2.1: Heat maps representing the activity of each radioisotope induced in copper via cosmogenic activation for various exposure, cooldown, and runtime combinations. Color bars are in units of counts/kg/day, and can vary from plot-to-plot by up to over two orders of magnitude.

The tritium activation rate is not well understood in copper, but it has been studied in silicon and germanium [4]. It is likely that an estimate of 1 atom per kilogram per day is smaller than the experimental value. Although its activity is smaller than every other isotope for a given exposure, cooldown, and runtime, it is evident that tritium contamination poses a pertinent long-term contribution to the experiment's background spectrum.

If SuperCDMS SNOLAB attains a similar operational reliability to that of SuperCDMS Soudan, runtimes can extend up to 19 months ($\sim$570 days). Also, many copper pieces (especially the copper cryostat) have now been exposed to cosmic rays at sea-level for above 1000 days. Therefore, the only practical option that permits a reduction in backgrounds originating from cosmogenic activation of copper is allowing pieces to cooldown for extended periods of time in the SNOLAB cavern. It is therefore paramount to develop a prescription for each component's cooldown time that conforms to the experiment's background budget.

Additionally, it is important to consider how the exposure of copper pieces that are closer to the detectors will influence backgrounds. For instance, a 100-day sea-level exposure of the detector housings is more concerning than an equivalent exposure of the OVC, since the latter is further from the detectors. In spite of the cryostat cans' larger mass, the distance and line-of-sight of a background source to the detectors generally have the most significant background impact.

2.3 Background Spectra for Technical Design Report Exposures and Cooldowns

Radiogenic backgrounds are modelled in SuperSim by uniformly contaminating the bulk of the experiment's copper instrumentation with particles that possess the characteristic energies of each radionuclide's decay daughters (colloquially referred to as

Table 2.2: Summary of expected background rates for detector-bulk single ER scatter events in the SuperCDMS SNOLAB experiment taken from [3]. Other sources of background which will have a nonzero but minute contribution, or contribute only to NR scatters, are marked as "-". Rates are calculated according to the ROI for each detector given in Table 1.1. The highlighted row will serve as the benchmark for this study.

ER Singles per kky	Si iZIP	Ge iZIP	Si HV	Ge HV
Coherent Neutrinos	-	-	-	-
Detector-Bulk Contamination	260.	8.5	290.	21
Material Activation	15.	1.9	2.5	1.0
Non-Line-of-Sight Surfaces	0.07	0.01	0.03	0.00
Bulk Material Contamination	88.	12.	14.	5.4
Cavern Environment	-	-	-	-
Cosmogenic Neutrons	-	-	-	-
Total	370.	22.	300.	27.

"primaries"). Detector response is handled by another part of the simulations chain, called the detector Monte Carlo (DMC). SuperSim provides Geant4 with the geometry and material description of the cryostat, towers, detector housings, electronics, and much more. This permits background studies emulating the parameters in Section 1.5 to be performed.

Reference [3] provides information on the assumed rates of single ER scatters in SuperCDMS SNOLAB. Those values will be used as a benchmark for the results obtained in this investigation. Therein, material activation accounts for ∼2.83% of bulk ER single events. However, the paper assumes that tower components have a 90-day SLE exposure and cooldown period while cryostat cans are subject to 180 days of SLE exposure and cooldown. The following section will explore the sensitivity of this fraction to different exposure and cooldown combinations.

To begin, we use the parameters from [3] (given in Table 2.3) to assess the consistency of both simulations. Spectral sums are tabulated in Table 2.4 and spectra are plotted in Figures 2.3 and 2.2. Note that the copper shield is assumed to have

Table 2.3: Assumed exposure, cooldown, and runtimes for copper parts of the SuperCDMS SNOLAB instrumentation. Results are plotted in Figure 2.3 and tabulated in Table 2.4.

	Exposure (d)	Cooldown (d)	Runtime (y)
Housing & Towers	90	90	5
Thermal Stages	90	90	5
MC, CP, ST, LH, OVC	180	180	5
Copper Shield	180	365	5
E-Stem & C-Stem	180	180	5

Table 2.4: Spectral Sums for each isotope induced in copper plotted in Figure 2.3. The sums are in in units of bulk ER singles per kky over the energy region of interest for each detector type in the SuperCDMS SNOLAB experiment. Energies reflect the recoil energy of an event, rather than their nuclear or electron recoil equivalent. Uncertainties are calculated assuming that the background spectra are Poissonian.

	Spectral Sums (Bulk ER Singles/kky)			
Isotope	Si iZIP	Ge iZIP	Si HV	Ge HV
^{60}Co	8.1 ± 0.1	2.697 ± 0.001	4.015 ± 0.006	1.706 ± 0.008
^{58}Co	1.09 ± 0.01	$0.3550 \pm 1\times10^{-4}$	0.602 ± 0.005	$0.2166 \pm 7\times10^{-4}$
^{57}Co	2.49 ± 0.04	$0.2326 \pm 1\times10^{-4}$	1.26 ± 0.01	0.085 ± 0.002
^{56}Co	0.259 ± 0.005	$0.08772 \pm 4\times10^{-5}$	$0.1352 \pm 7\times10^{-4}$	$0.059333 \pm 7\times10^{-4}$
^{59}Fe	0.073 ± 0.001	$0.024612 \pm 1\times10^{-5}$	$0.05203 \pm 8\times10^{-5}$	$0.01577 \pm 7\times10^{-5}$
^{54}Mn	0.53 ± 0.02	$0.1716 \pm 1\times10^{-4}$	0.324 ± 0.006	0.106 ± 0.003
^{46}Sc	0.051 ± 0.002	$0.01704 \pm 1\times10^{-5}$	$0.03539 \pm 5\times10^{-5}$	$0.0095 \pm 5\times10^{-4}$
Total	12.6 ± 0.2	3.568 ± 0.001	6.42 ± 0.03	3.11 ± 0.01

a 365-day cooldown period. This was chosen to be consistent with an internal study performed on cosmogenic activation in copper. The different cooldown affects the number of ERs and spectra minimally.

Notice that the aggregate spectrum in Figure 2.2 strongly resembles that of ^{60}Co from Figure 2.3. While the photopeaks from other isotopes are clearly visible, the aggregate spectrum most clearly displays the Compton edge, backscatter peak, and escape peaks characteristic of ^{60}Co's gamma spectrum. The isotope's relatively large production rate and half-life afford it a much stronger presence in this spectrum, which will become more evident once larger cooldown times are imposed.

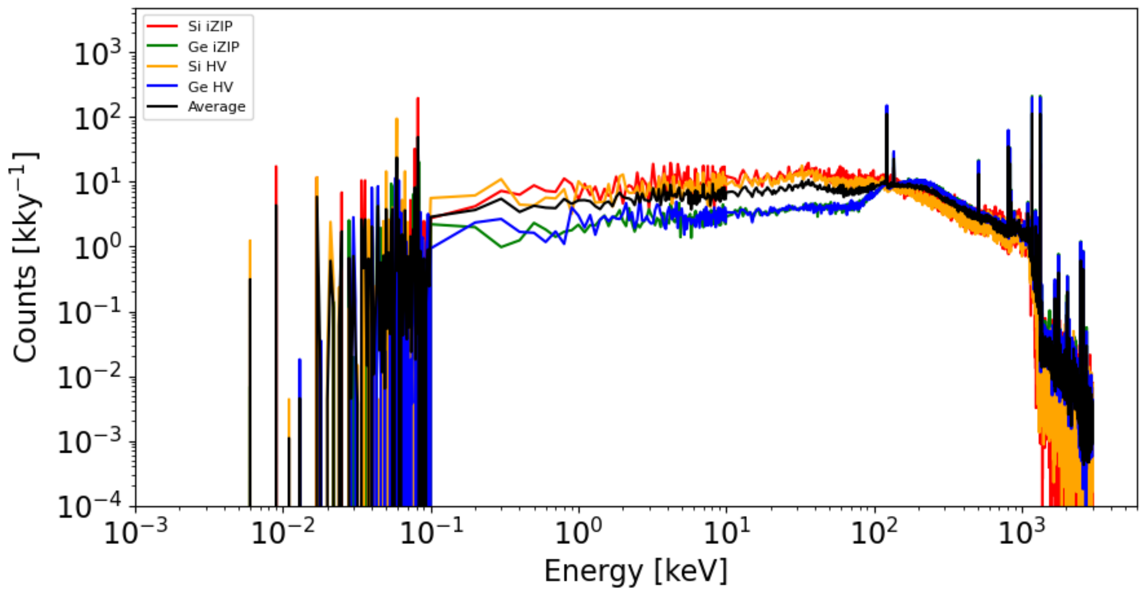

Figure 2.2: Total internal material activation spectrum originating from decay daughters of different radionuclides induced by cosmogenic activation in copper components of the SuperCDMS SNOLAB experiment. Signals are plotted for silicon iZIPs (red), germanium iZIPs (green), silicon HVs (orange), germanium HVs (blue), and the average of each spectrum is plotted in black. Assumptions on the exposure, cooldown, and live time are given in Table 2.3.

Another notable feature of Figure 2.2 is the "tail" that begins to dominate the spectrum in germanium detectors beginning at ~ 80 keV caused by the geometry of each detector stack. Each stack has a germanium detector at its top and bottom, which screen the other 4 detectors in their stack from decay daughters created in the lid and base of the cryostat. Figure 2.5 illustrates this shielding effect for backgrounds originating from ^{60}Co. While extra shielding from other detectors should not influence the shape of a spectrum, signals observed by silicon detectors are expected to be less frequent than those observed by germanium detectors for a given energy.

The "tail" in this case is simply a ~ 209 keV backscattering peak caused by primary photons originating from the experiment's inner instrumentation (e.g., housing or MC) undergoing Compton scattering at angles close to 180° in a component that is further away from the detectors (e.g., OVC or shielding). These rebounding pho-

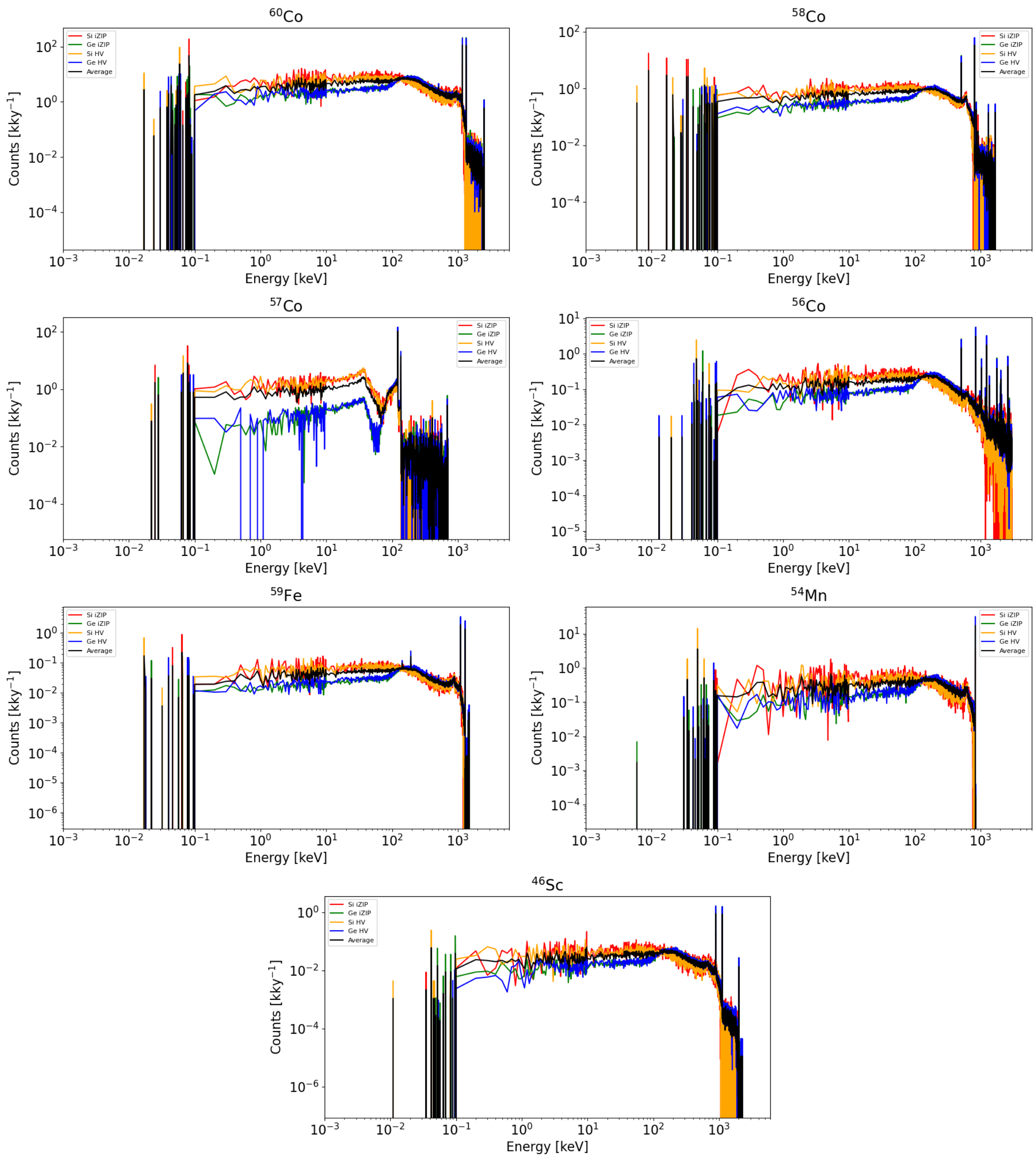

Figure 2.3: Background spectra originating from decay daughters of different radionuclides induced by cosmogenic activation in copper components of the SuperCDMS SNOLAB experiment. Signals are plotted for silicon iZIPs (red), germanium iZIPs (green), silicon HVs (orange), germanium HVs (blue), and the average of each spectrum is plotted in black. Assumptions on the exposure, cooldown, and live time are given in Table 2.3.

tons then have a chance to hit a detector. The peak appears smeared since it is not a "true" photopeak since Compton scattering can occur at multiple angles and contribute to a continuum of energies in the 80 - 250 keV region. It also appears stretched by the x-axis logarithmic scaling.

Additionally, the backscattering peak is not present in silicon detectors because of differing mean free paths in each crystal. For a 210 keV gamma, the mass attenuation coefficients for silicon and germanium are approximately 0.125 cm^2/g and 0.148 cm^2/g, respectively [21]. Therefore, the mean free path for 210 keV gamma is 3.4 cm in silicon and 1.3 cm in germanium. As a result, gammas are more likely to deposit all of their energy in a germanium detector through multiple Compton scattering. In contrast, the mean free path of gammas with energy characteristic of a backscattering peak in silicon is larger than the thickness of the detectors! Figure 2.4 plots photon energy loss through Compton scattering in each crystal type for primary gammas with energy above 200 keV, to illustrate this point.

The figure is normalized by the number of incident primaries with energies above 200 keV on the silicon and germanium detectors to provide a direct comparison between the rates in each crystal type. As can be seen in the figure, there is an approximately equal distribution of single Compton scatters in both the silicon and germanium crystals, with slightly more occuring in the 200 keV region for germanium. Similarly, the energy deposited via multiple Compton scattering tends to have slightly more counts in the 200 keV region for germanium detectors than silicon detectors. This suggests that the detectors' different mean free paths are the reason that backscattering peaks are absent from silicon detectors but not from germanium detectors in this study.

This analysis is not a quantitatively rigorous treatment of the issue. It is therefore possible that the backscattering peak is absent from each silicon spectrum for reasons

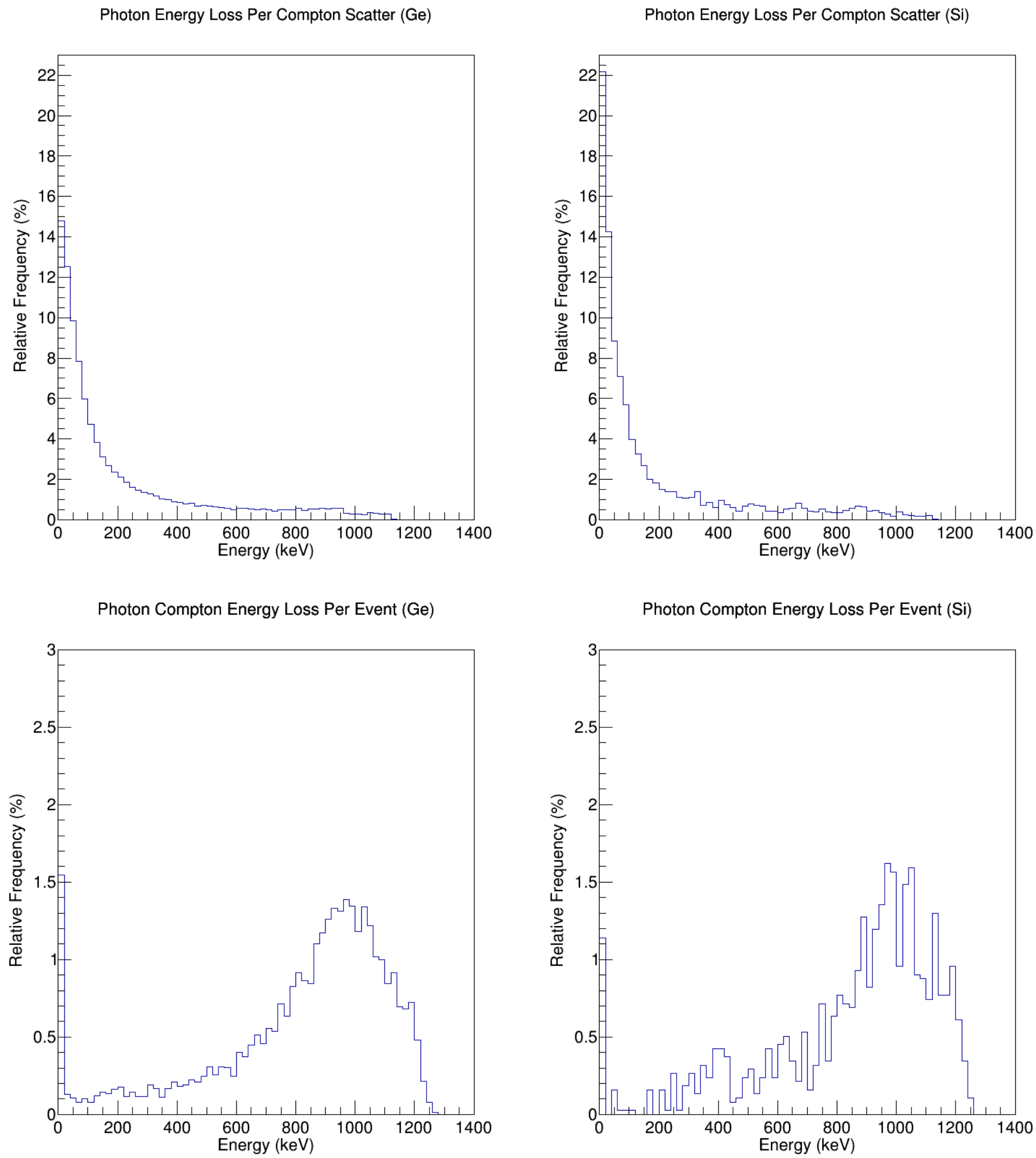

Figure 2.4: (Top) Simulated energy loss of photons originating from ^{60}Co decays in LH thermal stage copper incident on SuperCDMS SNOLAB germanium (left) and silicon (detectors) per Compton scatter. (Bottom) Simulated energy loss of photons originating from ^{60}Co decays in LH thermal stage copper incident on SuperCDMS SNOLAB germanium (left) and silicon (detectors) per simulated event. The histograms for silicon and germanium are normalized by the number of primary photons with energy greater than 1 MeV incident on each detector. The bottom row aggregates the energy loss from each event in the first row into a single bin. Results are obtained from SuperSim.

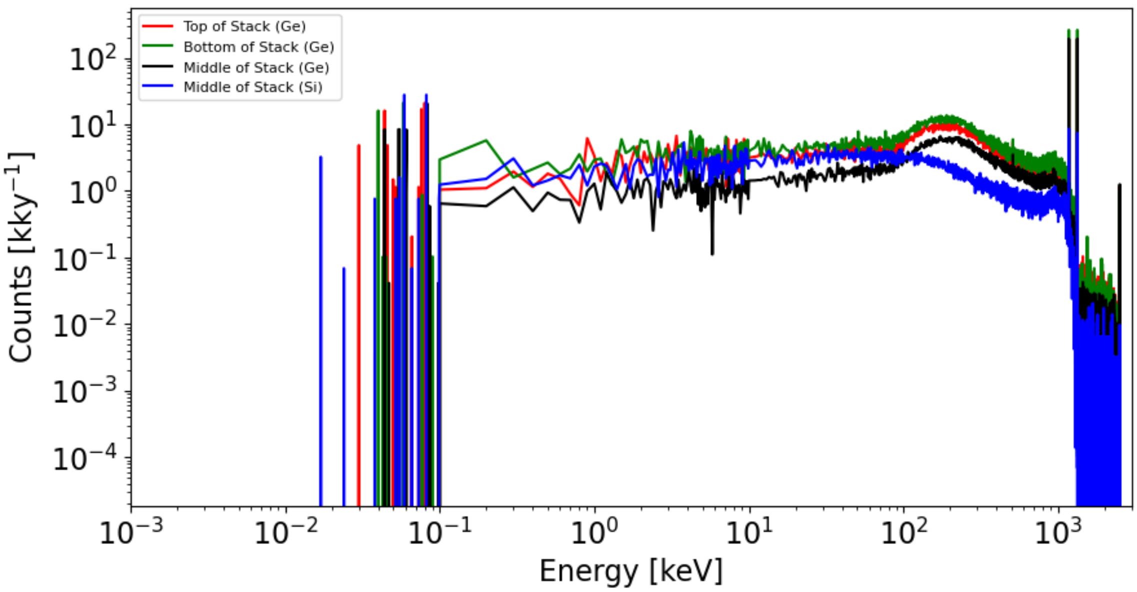

Figure 2.5: Spectrum of bulk ER singles per kky originating from ^{60}Co decays simulated in SuperSim for every detector in the SuperCDMS SNOLAB experiment at the top, bottom, and middle of each stack. Notice that the detectors in the top and bottom positions report a higher rate than those in the middle due to screening effects of detectors on either end of each stack. This spectrum assumes an identical crystal mass for germanium and silicon of 1.39 kg for the sake of direct comparison.

other than those explored here.

Importantly, [3] characterizes the cosmogenic activation of germanium in the detectors as "detector contamination" rather than material activation. Therefore, the mapping of copper components will be similar across both reports, with one caveat: in 2020, the collaboration redesigned the SNOBOX to be smaller due to a higher-than-anticipated cost and fabrication time. The redesign saw a reduced copper can radius, which also meant a decreased amount of material. The background impact is expected to decrease polynomially with the former and linearly with the latter, since detectors inside smaller cans occupy a larger solid angle. Given that ref. [3] was written in 2017, it uses the deprecated cryostat design. In addition, the background estimates are based on a populated 7-tower design which can provide more shielding for detectors and decrease background rates, but simultaneously introduce more material and increase background rates.

It is noted in ref. [3] that dedicated studies concluded the redesign did not significantly impact normalized event rates. Therefore, this report will follow suit and directly compare spectra in spite of the noted discrepancies.

Using the sums obtained from this investigation, cosmogenic activation would instead account for 3.55% of background events - a 0.69% increase from the benchmark. Uncertainties for each spectral sum are well below 5%, and they are calculated assuming that the background spectra are Poissonian. That is, the uncertainty for a bin containing N events (without a normalization factor applied) is given by $\sqrt{N}$. Therefore, the uncertainty for a spectral sum is recovered by adding the uncertainty of each bin in a spectrum in quadrature. This means that the uncertainty of the spectral sum is simply the square root of the non-normalized total number of events, which is then normalized according to equation 1.7.

The primary sources of disagreement between Table 2.4 and the benchmark are changes to the SuperSim geometry and fidelity since the time that the paper was written. Notably, the E-stem and C-stem were not incorporated in the benchmark study's simulations, several thermal stages did not feature the level of fidelity that SuperSim boasts today, and the cryostat had not been reduced in size.

Notice that the spectrum for ^{57}Co has a very discernible Compton edge. According to Table 2.1, ^{57}Co primarily emits 122 keV gammas, which can transfer a maximum of 40 keV in a backscattering event. Each other isotope in Figure 2.3 emits gammas in the ~ 1 MeV region. Therefore, their Compton edges, while visible typically just below 1 MeV, are difficult to discern due to the axis scaling.

Also note that each spectrum in 2.3 is dominated by signals observed in Si detectors in the 0.1-80 keV region. This is a result of the normalization scheme given by equation 1.7 and the low mass of each silicon detector compared to their germanium counterparts; 0.608 kg and 1.39 kg, respectively. If the masses in each detector are assumed to be equal, this discrepancy disappears.

As of this writing, no comprehensive assay of the exposure in the cryostat cans has been done in the last 5 years. Therefore, a set of general exposure and cooldown combinations will be assumed both to illustrate the effects of large exposures, and prescribe a pragmatic cooldown time to minimize background rates.

The collaboration's background control efforts would be bolstered by an exact determination of the exposure for each copper piece. The route that each detector tower took while it was shipped from SLAC to SNOLAB was thoroughly documented, which will allow for more detailed studies in the future. The same should be done for cryostat copper.

2.4 Background Spectra for Variable Exposures and Cooldowns

It is instructive to first assess how a large exposure and minimal cooldown would impact background rates. It is noted that exposure and cooldown times are somewhat grounded in reality, given that two towers reached the SNOLAB cavern in May, 2023, and another two went underground in November, 2023. To provide a more conservative estimate, it will be assumed that both sets of towers and housings reached the cavern in November, 2023. This will have the effect of both reducing their exposure and increasing their cooldown by approximately 210 days compared to the cryostat cans. It is additionally emphasized that each tower was stored in PNNL's SUL with a 16 m overburden, and so their exposures are not in reality sea-level equivalent. This is not considered here, and should be taken into account by developing a more detailed exposure history of the towers.

The SNOBOX copper exposure time was chosen based on a 2021 internal study which had examined background rates from SNOBOX copper. At the time, it was de-

Table 2.5: Assumed exposure, cooldown, and runtimes for copper parts of the SuperCDMS SNOLAB instrumentation with an increased exposure and minimal cooldown. Results are plotted in Figure 2.6 and tabulated in Table 2.6.

	Exposure (d)	Cooldown (d)	Runtime (y)
Housing & Towers	1060	390	5
Thermal Stages	1060	390	5
MC, CP, ST, LH, OVC	1270	180	5
Copper Shield	1270	180	5
E-Stem & C-Stem	1270	180	5

termined that with the cooldown times in Table 2.3, all commercially-sourced copper could be exposed to cosmic rays for 540 days for material internal activation not to exceed 10% of the experiment's background budget. As time has gone on and pieces remain above-ground, the exposure continues to grow. Therefore, it is assumed for this study that SNOBOX copper will now experience 540 days + 2 years = 1270 days of SLE exposure.

Figure 2.6, Table 2.5, and Table 2.6 provide information on the background spectra from cosmogenic activation given a 1270-day exposure in cryostat copper along with the known exposure and estimated cooldown of tower copper, similar to Table 2.3. With these new parameters, background events originating from cosmogenic activation would increase to 14.3% of the total observed background rate.

Notice in Table 2.6 that the majority of events are caused by ^{60}Co decay daughters due to the isotope's relatively large lifetime. Another large contributor is ^{57}Co, but its half-life is significantly smaller than that of ^{60}Co, and so any amount of cooldown time will cause a disparity between both rates. Likewise, ^{58}Co has a comparable production rate to ^{57}Co, but less than a third of the latter's half-life and a tenth of the rate.

Qualitatively, the spectra in Figure 2.6 do not differ significantly from those in Figure 2.3. In fact, exposure and cooldown contribute only to the scaling of the

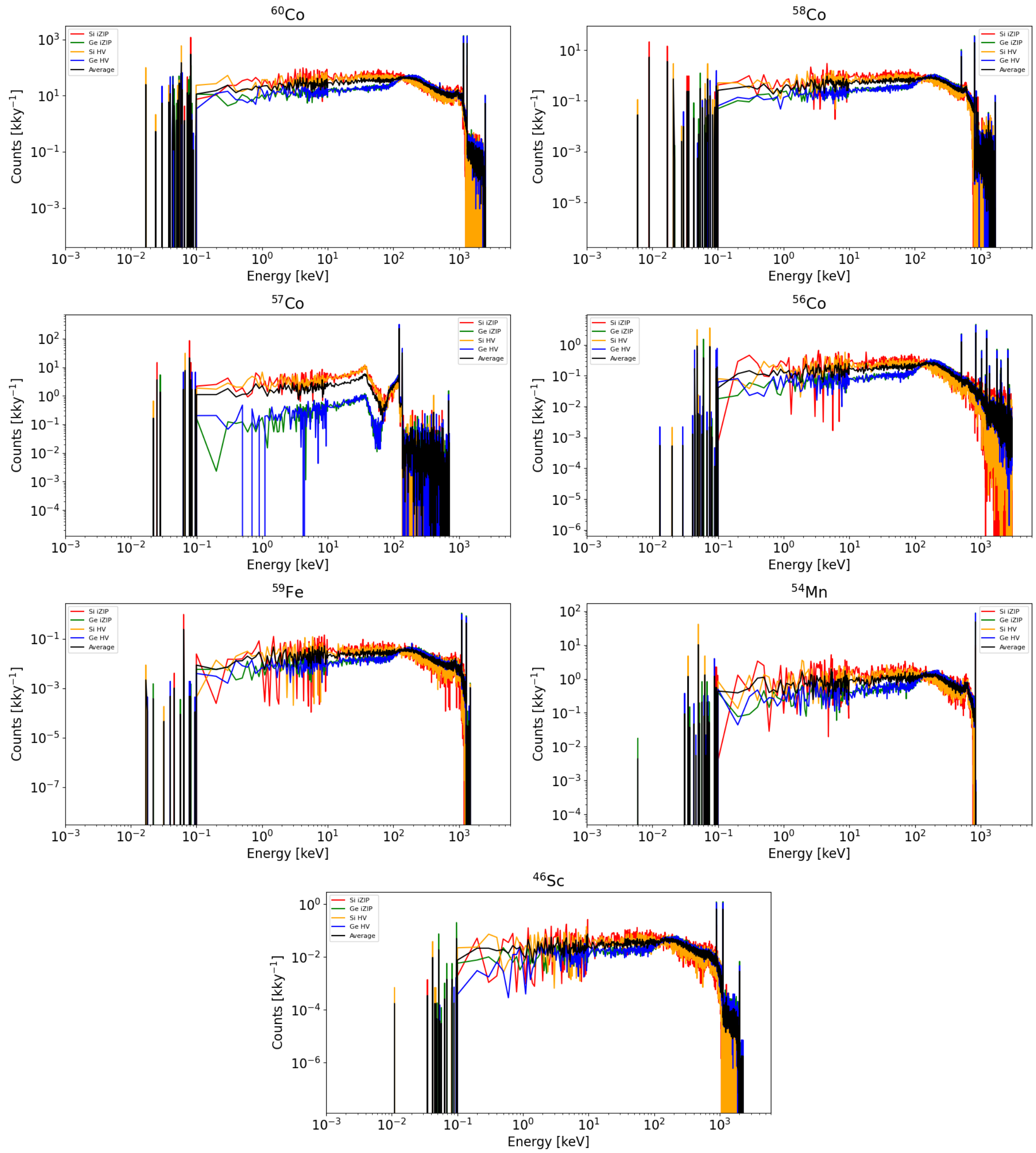

Figure 2.6: Background spectra originating from decay daughters of different radionuclides induced by cosmogenic activation in copper components of the SuperCDMS SNOLAB experiment. Signals are plotted for silicon iZIPs (red), germanium iZIPs (green), silicon HVs (orange), germanium HVs (blue), and the average of each spectrum is plotted in black. Assumptions on the exposure, cooldown, and live time are given in Table 2.5.

Table 2.6: Spectral Sums for each isotope induced in copper plotted in Figure 2.6. The sums are in in units of bulk ER singles per kky over the energy region of interest for each detector type in the SuperCDMS SNOLAB experiment. Uncertainties are calculated assuming that the background spectra are Poissonian.

	Spectral Sums (Bulk ER Singles/kky)			
Isotope	Si iZIP	Ge iZIP	Si HV	Ge HV
^{60}Co	49.5 ± 0.7	16.608 ± 0.006	24.98 ± 0.05	10.56 ± 0.04
^{58}Co	0.92 ± 0.01	0.2994 ± 1×10^{-4}	0.450 ± 0.004	0.1513 ± 8×10^{-4}
^{57}Co	5.45 ± 0.09	0.5119 ± 3×10^{-4}	2.76 ± 0.02	0.185 ± 0.003
^{56}Co	0.275 ± 0.006	0.09158 ± 5×10^{-5}	0.1311 ± 8×10^{-4}	0.0602644 ± 2×10^{-7}
^{59}Fe	0.037 ± 0.001	0.013051 ± 9×10^{-6}	0.022897 ± 1×10^{-6}	0.00704 ± 7×10^{-5}
^{54}Mn	1.51 ± 0.05	0.4846 ± 4×10^{-4}	0.92 ± 0.03	0.298 ± 0.008
^{46}Sc	0.050 ± 0.002	0.01658 ± 1×10^{-5}	0.033132 ± 8×10^{-6}	0.0084 ± 6×10^{-4}
Total	57.7 ± 0.9	18.025 ± 0.007	29.3 ± 0.1	11.27 ± 0.05

background rate, meaning that the shape of each spectrum will be identical. In light of this, individual spectra for each isotope will not be plotted for any other exposure and cooldown combinations, as it does not provide interesting information. However, these changes *would* have a pronounced effect in an aggregate background spectrum which displays each radioisotope's contribution.

Next, it is informative to examine the cooldown time required to observe a background rate comparable to that of the benchmark study. Table 2.7, and Table 2.8 show the background spectra, exposures and cooldowns, and spectral sums, respectively. With this set of parameters, material internal activation accounts for 2.9% of the total rate - approximately the same fraction as the benchmark study.

It is immediately clear that unless the entire cryotat is engineered again with new (i.e., recently extracted with limited exposure) copper, it is *extremely* impractical to allow each piece to cool down to a similar activity as in Table 2.3, which prescribed a roughly 13-year cooldown period. Therefore, it is prudent to determine a pragmatic cooldown and runtime given the current assumed exposure that will minimize this source of background. Cosmogenic activation produces several sources of background in the ~1 keV region and below, which can adversely impact the experiment's sen-

Table 2.7: Assumed exposure, cooldown, and runtimes for copper parts of the SuperCDMS SNOLAB instrumentation with an increased exposure and cooldown that will recover the same background rates as in the benchmark study. Results are tabulated in Table 2.8.

	Exposure (d)	Cooldown (d)	Runtime (y)
Housing & Towers	1060	4700	5
Thermal Stages	1060	4700	5
MC, CP, ST, LH, OVC	1270	4910	5
Copper Shield	1270	4910	5
E-Stem & C-Stem	1270	4910	5

sitivity to sub-GeV mass DM. The extent of this impact is not treated numerically here.

Notice that, consistent with what was predicted from Figure 2.1, the background contribution in Table 2.7 is dominated by ^{60}Co. This stands in contrast to the spectra obtained from the previous set of exposure and cooldown times, which featured non-negligible contributions from isotopes with large exposure times such as ^{57}Co. However, now that a larger cooldown time has been imposed, most of the isotopes' short half-lives limit their contributions significantly.

An auxiliary benefit to a relatively large cooldown time is that background spectra become easier to understand and subtract from the total event rate. That is, since the spectral sums in Table 2.8 are dominated by contributions from ^{60}Co daughters which have an easily-identifiable spectrum, it is less difficult to discern which peaks originate from certain background sources in aggregate spectra. This stark difference is illustrated in Figure 2.7, which strongly resembles the ^{60}Co spectrum.

A reasonable background level for cosmogenic activation is 10% of the total observed rate. The required cooldown time to achieve this is given in Table 2.9, and the spectral sums are tabulated in 2.10. While a 2.5-year cooldown period is more reasonable than the previous scenario's prescription, it would nonetheless demand that the experiment begin taking data at a significantly later time than anticipated.

Table 2.8: Spectral Sums for each isotope induced in copper given the assumptions on exposure and cooldown in Table 2.7. The sums are in in units of bulk ER singles per kky over the energy region of interest for each detector type in the SuperCDMS SNOLAB experiment. Uncertainties are calculated assuming that the background spectra are Poissonian. Isotopes which contribute $< 10^5$ ER singles/kky are excluded.

	Spectral Sums (Bulk ER Singles/kky)			
Isotope	Si iZIP	Ge iZIP	Si HV	Ge HV
^{60}Co	9.2 ± 0.1	3.09 ± 0.001	4.67 ± 0.01	1.970 ± 0.008
^{58}Co	-	-	-	-
^{57}Co	$(81 \pm 1)\times10^{-6}$	-	$(415 \pm 4)\times10^{-7}$	$(2821 \pm 6)\times10^{-8}$
^{56}Co	-	-	-	-
^{59}Fe	-	-	-	-
^{54}Mn	$(55 \pm 1)\times10^{-6}$	$(1783 \pm 1)\times10^{-8}$	$(350 \pm 7)\times10^{-4}$	$(118 \pm 2)\times10^{-7}$
^{46}Sc	-	-	-	-
Total	9.2 ± 0.1	3.09 ± 0.001	4.67 ± 0.01	1.970 ± 0.008

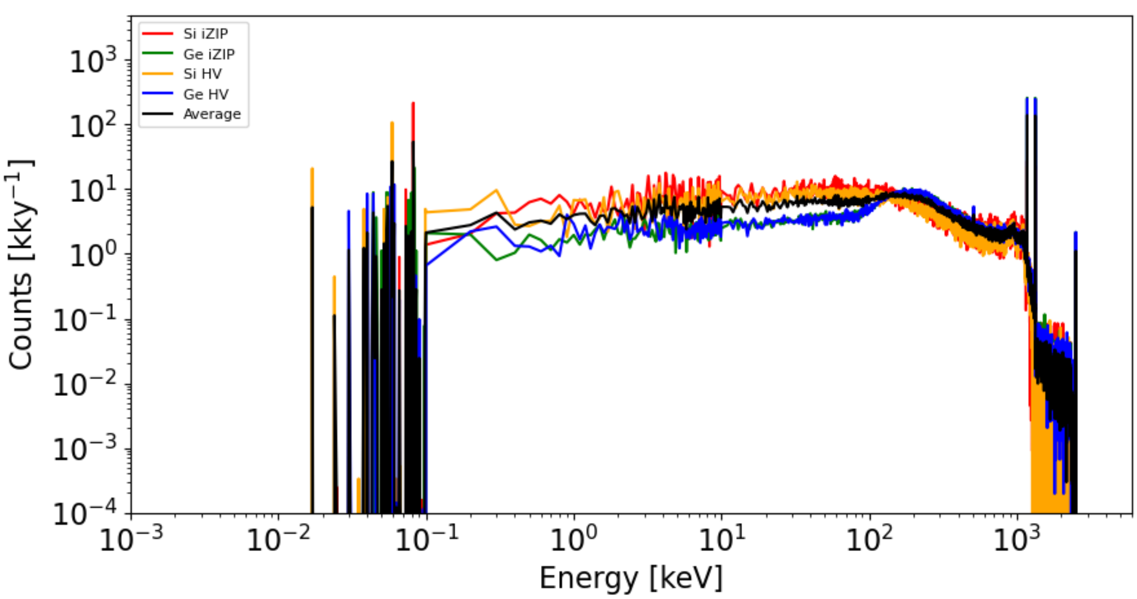

Figure 2.7: Total internal material activation spectrum originating from decay daughters of different radionuclides induced by cosmogenic activation in copper components of the SuperCDMS SNOLAB experiment. Signals are plotted for silicon iZIPs (red), germanium iZIPs (green), silicon HVs (orange), germanium HVs (blue), and the average of each spectrum is plotted in black. Assumptions on the exposure, cooldown, and live time are given in Table 2.7. Notice the strikingly similar spectrographic features to those of ^{60}Co.

Table 2.9: Assumed exposure, cooldown, and runtimes for copper parts of the SuperCDMS SNOLAB instrumentation that will result in material internal activation accounting for 10% of the experiment's total background rate. Results are tabulated in Table 2.10.

	Exposure (d)	Cooldown (d)	Runtime (y)
Housing & Towers	1060	900	5
Thermal Stages	1060	900	5
MC, CP, ST, LH, OVC	1270	1110	5
Copper Shield	1270	1110	5
E-Stem & C-Stem	1270	1110	5

Table 2.10: Spectral Sums for each isotope induced in copper plotted in given the assumptions on exposure and cooldown in Table 2.9. The sums are in in units of bulk ER singles per kky over the energy region of interest for each detector type in the SuperCDMS SNOLAB experiment. Uncertainties are calculated assuming that the background spectra are Poissonian. Isotopes which contribute $< 10^5$ ER singles/kky are excluded.

	Spectral Sums (Bulk ER Singles/kky)			
Isotope	Si iZIP	Ge iZIP	Si HV	Ge HV
^{60}Co	36.1 ± 0.5	12.145 ± 0.004	18.34 ± 0.04	7.74 ± 0.03
^{58}Co	$(343 \pm 5)\times10^{-6}$	$(11155 \pm 3)\times10^{-8}$	$(220 \pm 2)\times10^{-6}$	$(805 \pm 2)\times10^{-6}$
^{57}Co	1.31 ± 0.02	$0.12106 \pm 4\times10^{-5}$	0.670 ± 0.006	$0.0455 \pm 9\times10^{-4}$
^{56}Co	$(134 \pm 2)\times10^{-6}$	$(4643 \pm 2)\times10^{-8}$	$(758 \pm 6)\times10^{-7}$	$(31623 \pm 2)\times10^{-9}$
^{59}Fe	-	-	-	-
^{54}Mn	0.255 ± 0.006	$0.08204 \pm 5\times10^{-5}$	1.61 ± 0.003	0.054 ± 0.001
^{46}Sc	$(57 \pm 1)\times10^{-6}$	$(19534 \pm 7)\times10^{-9}$	$(419 \pm 1)\times10^{-7}$	$(116 \pm 3)\times10^{-7}$
Total	37.7 ± 0.5	12.348 ± 0.004	20.62 ± 0.05	7.84 ± 0.03

Given that any increase in the cooldown time of SNOBOX copper will result in disruptive delays to the experiment's schedule, it is recommended that the SuperCDMS collaboration allows cosmogenic activation to account for up to 15% of its background (corresponding to the exposures and cooldowns given in Table 2.3) for a 5-year data-taking period. As of this writing, the cryostat cans for the experiment have already been fabricated and are being prepared for shipping to SNOLAB. Therefore, it is equally as impractical and disruptive to fabricate new cryostat cans and towers in order to mitigate this source of background.

While it is imperative to reduce the number of background events in DM searches, it is also important to estimate each source of background in order to understand the feasibility of abiding by the experiment's background budget and running schedule. This investigation has shown that reducing the experiment's background rate originating from radionuclides induced through cosmogenic activation is costly, disruptive, and unrealistic. It is therefore reasonable to look to other sources of background in the experiment and assess how feasible it is to control them more stringently than previously thought necessary.

Chapter 3

Production Cuts in Geant4 and SuperSim

This chapter will characterize and investigate a software issue concerning production cuts and safety for electromagnetic processes in SuperSim.

Geant4 ships with numerous examples featuring custom classes that demonstrate basic use cases for the toolkit. One such example is `TestEm5`, which models multiple Coulomb scattering due to particle transport and provides information such as interaction cross sections, counts of secondary particles, and stopping powers. Using these custom classes as a foundation for the investigation, Geant4's (version 10.6) production cuts and safety features are explored. These results, in conjunction with output from SuperSim, are analyzed to determine if safety is working as it is advertised in the documentation and used to inform unsuccessful attempts at resolving the issue. Finally, next steps for further investigation are prescribed.

3.1 Description of Production Cuts and Safety in Geant4

Geant4 is a C++-based simulations toolkit that is capable of modelling the passage of SM particles through matter. It is the foundation of the SuperCDMS collaboration's simulation package SuperSim, which uses custom classes, geometries, and the `Shielding` physics list in Geant4 to conduct background studies for the experiment [3]. It is important to emphasize that many crucial physics processes are the same in Geant4 and SuperSim, meaning that production cuts are expected to behave identically in both packages.

A particularly resource-intensive step in the simulations production chain is the

DMC, which models detector physics and response. This can include processes such as electron-hole pair creation and propagation, the NTL effect [3], and readout electronics.

However, simulating detector physics at a high level of detail comes with the cost of long runtimes. Not only is this an inconvenience, but the collaboration is granted a finite number of core-years on various high-performance computer clusters that are best used sparingly. To circumvent this issue, Geant4 ships with an option that allows users to neglect simulation of low-energy secondary particles (see the following section). This so-called production cuts mechanism would reduce DMC runtimes by not simulating low-energy x-rays or Auger electrons produced by the photoelectric effect.

That is, when a photoelectron is ejected from its inner shell by an incident photon, a low-energy x-ray or Auger electron may also be produced due to an outer shell electron filling the vacancy. These low-energy particles can sometimes escape the detector, resulting in a second "escape peak" that is lower in energy than the photopeak. The implementation of production cuts would cause these low-energy particles to be counted as energy depositions in the detector. Effectively, the photopeak and escape peak would become coincident for significant background event sources such as incident $\sim$8 keV copper x-ray emissions or cosmogenic activation lines in Ge detectors.

3.1.1 Production Cuts

Electromagnetically charged particles and photons travelling through a volume of material can generate a cascade of secondary particles through processes such as Compton scattering, the photoelectric effect, and atomic excitation. While tracking each secondary to zero range (defined in Geant4 by default as 990 eV, so as to avoid infrared divergences in electromagnetic processes) would result in high-accuracy

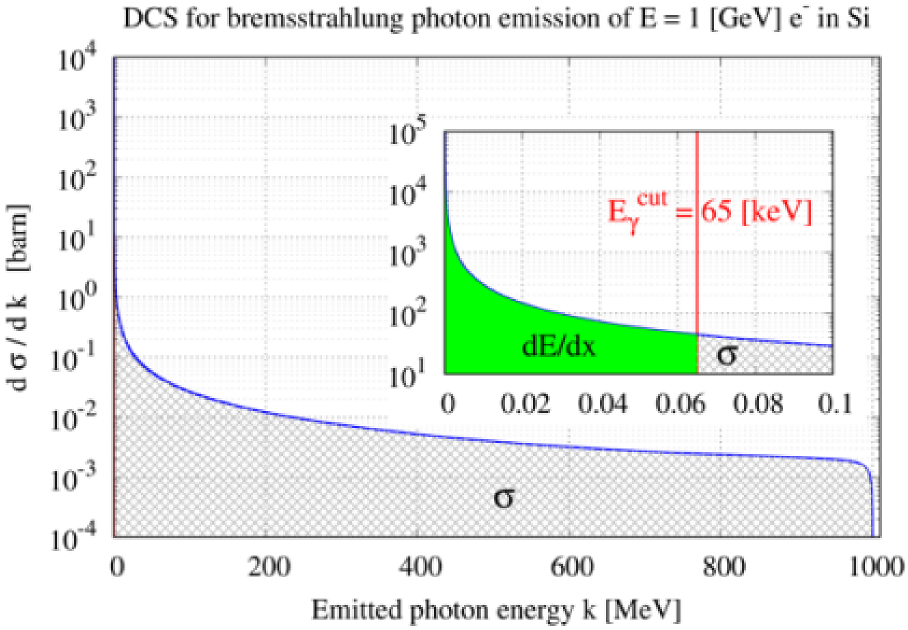

Figure 3.1: Graph of the Differential Cross Section (DCS) of bremmstrahlung photons generated by 1 GeV electrons in silicon. The inset graph illustrates the same differential cross section, but with an x-axis upper limit of 0.1 MeV. The region highlighted in green represents the energies of photons below a 65 keV production cut which are counted as energy depositions. Equation 3.1 shows how the energy deposition is related to the differential cross section [26].

simulation, it is not always pragmatic or necessary.

Take for example a low-energy bremmstrahlung photon created in a large volume of silicon. If its attenuation length is smaller than the spatial resolution of the detector, then CPU time would be wasted tracking a photon which the detector could not observe. In this case, imposing a production cut would decrease CPU time while minimally affecting simulation accuracy.

Secondaries possessing an energy smaller than the production threshold specified before beginning the simulation are not tracked and instead counted as an energy deposition. This process is illustrated in Figure 3.1; a production cut of 65 keV is imposed on bremmstrahlung photons in silicon, precluding the need to track any that are produced with an energy less than 65 keV. Note that production cuts are passed as lengths, which are subsequently converted into energy thresholds depending on the material of the current volume. The default production cut value for Geant4 reference physics lists is 0.7 mm.

Mathematically, we may characterize the mean energy stopping power in a volume resulting from a production cut E_{cut} as [26],

$$\frac{dE}{dx}(E_0, E_{\text{cut}}) = \mathcal{N} \int_{E_0=0}^{E_{\text{cut}}} k \frac{d\sigma}{dk} dk, \tag{3.1}$$

where $\mathcal{N}$ is a normalization constant, k is the energy of the emitted secondary particle, and σ is the cross section for a specific process (e.g., bremsstrahlung, as in the above example). It follows that a well-defined emission rate for secondaries above the production threshold is given by [26],

$$\sigma(E_{\text{cut}}, E_{\text{max}}) = \int_{E_{\text{cut}}}^{E_{\text{max}}} \frac{d\sigma}{dk} dk, \tag{3.2}$$

for some upper limit on secondary energies E.

3.1.2 Safety

While production cuts can reduce simulation time, implementing them throughout an entire volume can inaccurately model potentially interesting events. For example, it is desirable to track a secondary particle which is generated below the production cut but near an external volume boundary with the detector.

For this reason, Geant4 will dynamically (i.e., at the beginning of each step) calculate a quantity called safety: The shortest distance from a secondary to the closest volume boundary. Safety is subsequently compared to the production cut, and newly-generated secondary particles (that is, ones that have not yet taken a step) will be stacked (i.e., scheduled for further tracking) if the following condition is true:

$$\text{range} > \min(\text{safety, production cut}). \tag{3.3}$$

That is, if a secondary possesses a sufficiently large energy to reach the volume boundary, it will be stacked independently of the production cut. Therefore, a production cut may still be imposed to reduce simulation time while simultaneously tracking all potentially important events, regardless of their energy.

3.2 The Issue of Safety vs. Production Cuts in Geant4

Geant4 documentation describes the safety mechanism as defined above to work differently than it does in practice. For reasons that will be explored in this report, safety is not observed to prevent electromagnetically neutral secondary particles from being cut if they meet condition 3.3. While this does not render the production cuts mechanism useless, impetus to impose a production threshold is diminished; particularly for discrete processes whose cross sections are dominated at low energies.

To illustrate this issue, TestEm5 (which uses Geant4's standard electromagnetic physics list, option 4) is used to simulate 10^6 events with 2 MeV photons travelling perpendicularly to the 1 m $\times$ 1 m transverse face of a copper absorber. The absorber is 0.1 m thick and primary photons are shot along this axis (i.e., perpendicularly to the face of the absorber) from the center of the volume. Figure 3.2 illustrates the energy of neutral secondaries at creation for different production cut values in this geometry. Note that the "number of secondaries per event" refers to the total number of secondaries that are recopied to the temporary stack for later tracking (i.e., the integral under the histogram with no production cuts) in the simulation divided by the total number of primaries thrown. The former quantity is not the same as the number of secondaries which escape the volume; it is less than or equal to this number.

As photons travel through the copper, they generate photons, electrons, and positrons through "destructive" processes such as the photoelectric effect, Compton scattering, and pair production (i.e., those which change the energy of a photon). Production cuts are expected to apply independently to secondaries generated in each of these processes, with one exception: Geant4's `G4EmParameters` class provides an option for secondaries generated by atomic deexcitation processes to ignore cuts altogether. To fully characterize the issue in question, this option has been toggled off.

The `AbsorptionLength` vector of a photon in a given material is approximated by the sum of each destructive cross section for a given energy by the following formula:

$$L_{\text{abs}} = \frac{5}{\sigma_{\text{abs}}}, \tag{3.4}$$

where the factor of 5 comes from requiring that the probability of a non-destructive process occurring is small. Notice that this quantity is formulated similarly to the mean free path.

From the Beer-Lambert law, the probability for one of these processes *not* to occur is given by,

$$e^{-\sigma_{\text{abs}} L_{\text{abs}}} = e^{-5} = 6.7 \times 10^{-3}. \tag{3.5}$$

The quantity L_{abs} is important in determining the range of a photon in a given material. Henceforth, the "range" of a photon will refer to this quantity.

In the left histogram of Figure 3.2, there are 716995 neutral secondaries produced, with approximately 35% of them generated through atomic excitation of the 8.05

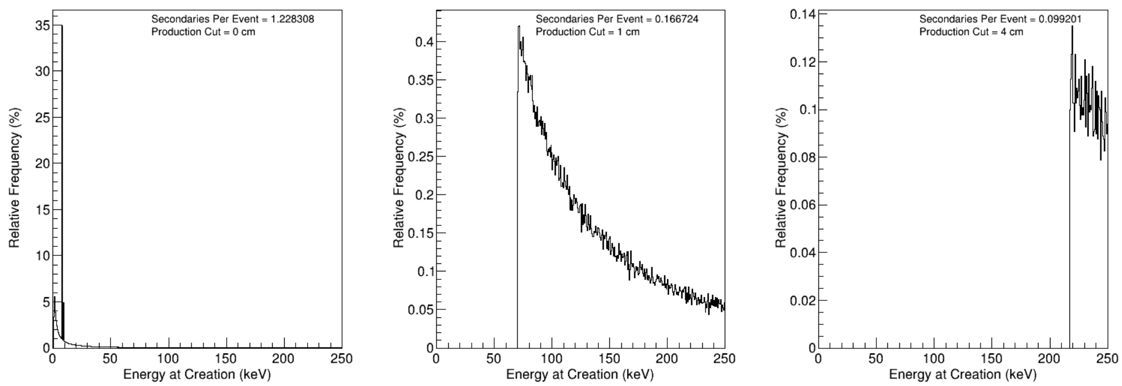

Figure 3.2: Geant4: Histograms showing the energy at creation of neutral secondaries in a 10 cm thick copper absorber resulting from 10^6 incident photons carrying an energy of 2 MeV with (left) a 0 μm production cut, (middle) a 1 cm production cut, and (right) a 4 cm production cut. A production threshold of 118 μm in copper is equivalent to a photon energy of 8 keV, whereas 1 cm and 4 cm are equivalent to 70 keV and 216 keV, respectively. The number of secondaries per event is given by the quotient of the number of secondaries created and number of incident primaries.

keV x-ray line in copper [34]. Assuming that there are 8.05 keV photons produced throughout the absorber, we would expect to see all of those that are produced within the safety. To make this inference more quantitative, we can estimate a lower limit on the number of 8.05 keV photons produced in the middle and right distributions of Figure 3.2 and compare it to the number of secondaries observed in each to assess the accuracy of simulation.

To do this, we note that for unpolarized, unscattered primaries, we expect a reduction in the rate of neutral secondaries produced on this x-ray line proportional to the number secondaries that are below the production threshold of 70 keV (for the case of the middle histogram) and are also generated outside of the safety.

Checking the range-to-energy conversion in the table of registered couples obtained by toggling on run verbosity reveals that the kα_1 x-ray energy of 8.05 keV in copper corresponds to a photon range (i.e., equation 3.4) of 119 μm. A 1 cm production cut should prevent stacking of every neutral secondary possessing less than 70 keV which is produced more than 1cm cm away from any boundary. Equally, any 8.05 keV photon which is produced more than 119 μm away from the absorber boundary will also be cut, since they are below the production threshold. Given the large transverse dimensions of the copper absorber, it is reasonable to only consider this distance along its shorter (i.e., 10 cm) side. Therefore, the fraction of the absorber in which neutral secondaries with an energy less than or equal to 8.05 keV would *not* be generated is:

$$\frac{5 \times 10^4\ \mu\text{m} - 119\ \mu\text{m}}{5 \times 10^4\ \mu\text{m}}$$
$$= 0.998.$$

Therefore, photons with energy less than 8.05 keV which are produced in 99.8% of the absorber's bulk are expected to be counted as energy depositions since they have insufficient energy to reach the volume boundary. In other words, they are outside of the safety.

Next, it is important to find the mean free path for a 2 MeV photon travelling through copper in order to calculate its extinction probability. This is straightforwardly calculated by Geant4's `TestEm14`: this example kills events at the first primary interaction and averages the track length from each to approximate the mean free path of a particle in various absorbers. It was found that the mean free path of a 2 MeV gamma through copper is approximately 2.8 cm. The extinction probability of a photon travelling through $\sim$5 cm of copper is then $e^{-5/2.69} = 0.16$.

The Monte Carlo result agrees well with ref. [21], which predicts a mass attenuation coefficient of $\sim$0.0399 cm^2/g for a 2 MeV photon in copper. Using the latter value and the mass density of copper, the mean free path is also found to be $0.0399^{-1} \times 8.935^{-1} = 2.8$ cm.

On the 8.05 keV line, we would then expect the number of secondaries produced to be:

$$(1 - 0.998) \times 0.16 \times 0.35 \times 1228308 \approx \boxed{136 \ \text{secondaries}}$$

Also note that this calculation is an underestimation. It assumes that only unscattered primaries can generate secondaries, but any primary that has an energy greater than 8.05 keV can generate secondaries on the copper kα_1 line.

This result is not consistent with the middle histogram in Figure 3.2, which shows that no secondaries are produced below 70 keV (corresponding exactly to the cut threshold). Furthermore, another reduction in the rate of secondary production is observed in the right histogram; once again, no secondaries are produced below the production threshold of 216 keV. As a result, production cuts do not appear to respect safety for neutral secondaries.

In contrast, a non-zero number of *charged* secondaries are observed below the production threshold with the same geometry in Figure 3.3. It is clear that production cuts impact the production rate of charged secondaries since there is a ~97% decrease in the number of secondaries per event when comparing the leftmost histogram with the middle histogram.

The discrepancy in secondary production rates between the middle and rightmost histograms of Figure 3.3 is not consistent with the behaviour expected from increasing the production threshold in this geometry. If we assume that the primary photon's entire 2 MeV of energy is transferred to a secondary electron, its attenuation length, according to the table of registered couples obtained using the physics list that ships with `TestEm5`, is $\sim$ 1.5 mm.

Meanwhile, the same table indicates that an electron possessing $\sim$ 14.6 MeV would be attenuated in 1 cm of copper, and an electron possessing $\sim$ 74.0 MeV would be

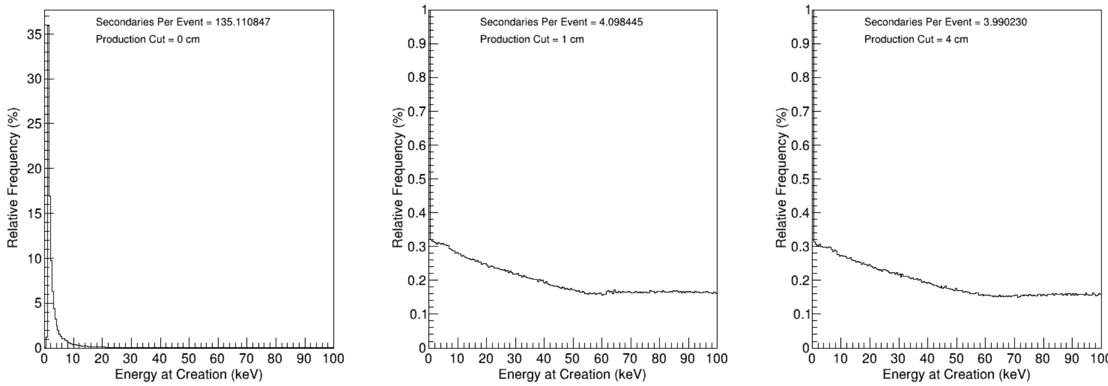

Figure 3.3: Geant4: Histograms showing the energy at creation of charged secondaries in a 10 cm thick copper absorber resulting from 10^6 incident photons carrying an energy of 2 MeV with (left) no production cuts applied, (middle) a 1 cm production cut applied, and (right) a 4 cm production cut applied. A production threshold of 1 cm in copper is equivalent to an electron energy of 14.6 MeV and a positron energy of 13.6 MeV, whereas a threshold of 4 cm is equivalent to an electron energy of 74.0 MeV and a positron energy of 69.2 MeV. The number of secondaries per event is given by the quotient of the number of secondaries created and number of incident primaries.

attenuated in 4 cm. Since a secondary electron in this setup cannot possess above 2 MeV of energy, the only way one should be stacked is if it is within at most 1.5 mm of the absorber's boundary (i.e., within safety). Therefore, no physically meaningful difference in the rates of surviving secondaries is expected between both scenarios. The same argument holds for positrons, albeit with slightly different attenuation lengths.

Furthermore, additional simulations employing production cut values of 2, 3, and 4.5 cm reported that the corresponding number of secondaries per event were 4.0, 4.0, and 3.9, respectively. This would suggest that the discrepancy results from the random nature of Monte Carlo simulation, and warrants no further attention.

Given that 2 MeV photons are most likely to produce charged secondaries via Compton scattering [36], let us perform the same analysis as the neutral case to determine a lower limit on the expected production rate. Note that the rate of positron production at this primary energy is a factor of 100 smaller than that for electrons, so accuracy is minimally affected by excluding pair production from this calculation.

Through integrating the well-known Klein-Nishina formula [33], we can calculate the median scattering angle for 2 MeV photons. The angle was determined to be 49.7° in Appendix B, so the median energy that is imparted to an electron via Compton scattering through this angle is,

$$\begin{aligned} E_e^{\max} &= E_\gamma \left(1 - \frac{1}{1 + \frac{E_\gamma}{m_e}(1 - \cos\theta)}\right) \\ &= 2 \text{ MeV} \left(1 - \frac{1}{1 + \frac{2 \text{ MeV}}{0.511 \text{ MeV}}(1 - \cos 49.7°)}\right) \\ &\approx 1.15 \text{ MeV}. \end{aligned}$$

It is also interesting to compare with the *mean* energy of electrons generated through Compton scattering obtained from `TestEm14`. By deactivating each other "destructive" process, it was found using this example that the mean electron energy from Compton scattering is ~ 1.05 MeV, which does not differ significantly from the above.

By checking the range-to-energy conversion in the table of registered couples, it can be verified that the above electron energy converts roughly to 797 μm in copper, meaning that 98.4% of electrons with an energy of 1.15 MeV will be produced outside of safety. This yields a production rate of $(1 - 0.984) \times 135 \times 0.16 \approx 0.346$ charged secondaries per event. This is a substantial underestimation compared to a rate of ~ 4.1 secondaries per event from the middle distribution of Figure 3.3. This is once again because only unscattered photons have been considered. For this reason, it is more compelling to consider the qualitative features of each spectrum.

That is, regardless of the exact value for each rate in the middle and right distributions, the presence of *any* charged secondaries in spite of a production threshold which is greater than their largest possible range is evidence that production cuts are not being applied to every secondary. Furthermore, the minute discrepancy between the middle and rightmost histograms suggests that different production cuts that are both larger than the absorber change the charged secondary production rate by a constant factor. This further suggests that Figure 3.3 illustrates that safety is allowing charged particles which are below threshold to be stacked.

From this, it is evident that the safety mechanism is not working as intended for neutral secondaries in Geant4, while it is working as expected for charged secondaries. A similar investigation was carried out in lead and germanium and in Geant4 versions 10.7 and 11.0. Results in each case were very similar to the above.

SuperSim appears to suffer from the same issue, as evidenced by the histograms in Figure 3.4. The above simulation shot 10^4 photons from ^{60}Co decay (primary energies of 1173 keV and 1333 keV) radially inwards along the surface of a 10 cm radius sphere at a germanium iZIP detector [7] inside its copper housing. While the geometry in this case differs from that used in Geant4, the observed spectra and the effect of production cuts on them are strikingly similar.

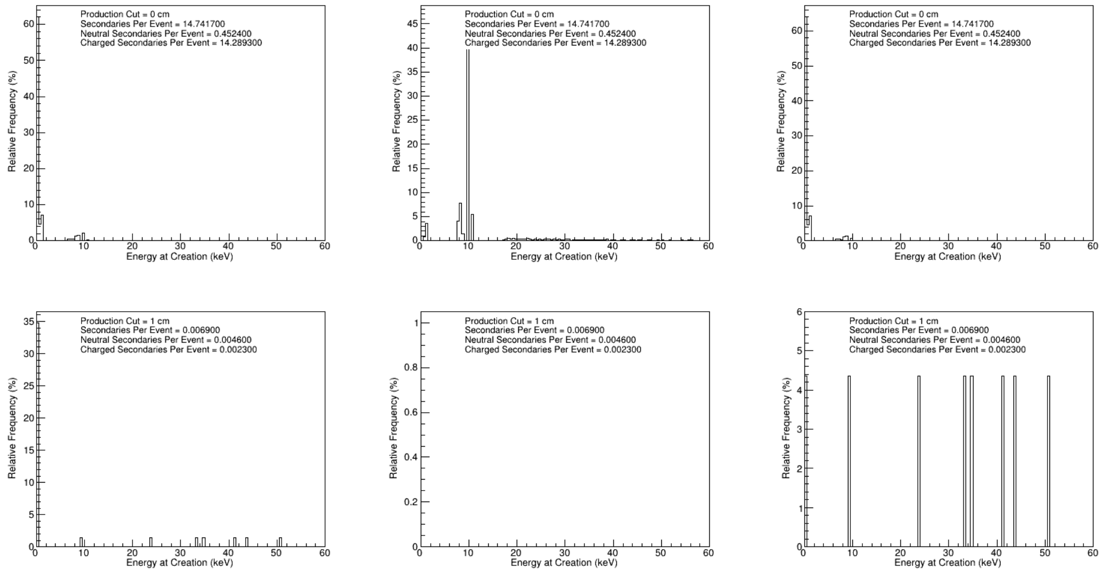

Figure 3.4: SuperSim: (left column) histograms showing the energy at creation of all secondaries in an iZIP detector + housing with no production cuts and a 1 cm production cut, (middle column) histograms showing the energy at creation of neutral secondaries in an iZIP detector + housing with no production cuts and a 1 cm production cut, (right column) histograms showing the energy at creation of all secondaries in an iZIP detector + housing with no production cuts and a 1 cm production cut. In each case, histograms with non-zero production cuts are in the bottom row.

3.3 Investigation of Geant4 Source Code

3.3.1 Calculation of Safety

Before checking if condition 3.3 was being handled correctly by Geant4, it was important to verify that both quantities in the comparison were calculated correctly. The process was trivial for production cuts; this quantity is specified at the beginning of a simulation and does not change. Conversely, the safety calculation was verified by toggling on higher verbosity options in the geometry navigator. Through adding the following preprocessor directive to the `G4Navigator` class constructor: `#define G4DebugNavigation ON`, the global position and safety of each secondary were printed.

```
**************************************************************************************************
* G4Track Information:   Particle = gamma,   Track ID = 9,   Parent ID = 1
**************************************************************************************************

Step#      X         Y         Z        KineE      dEStep     StepLeng    TrakLeng    Volume    Process
    0  -1.34 mm   1.91 mm  -1.38 cm   8.86 keV       0 eV        0 fm        0 fm   Absorber  initStep
*** G4Navigator::ComputeStep: ***
    Volume = Absorber - Proposed step length = 0.0229833
  Called with the arguments:
  Globalpoint =                      (-1.33808,1.91407,-13.7649)
  Direction   =                      (-0.941184,-0.0600074,0.332522)
  Returned step= 9e+99 Requested step= 0.0229833  Safety = 48.6619
    1  -1.36 mm   1.91 mm  -1.38 cm      0 eV     1.09 keV       23 um       23 um   Absorber  phot
```

Figure 3.5: Snapshot of verbose output from shooting a 2 MeV gamma along the 0.1 cm long side of the familiar copper absorber, from its center. Since the centre of the absorber is located at the world origin, GlobalPoint gives an accurate position for secondaries in both the world and absorber. Note that unless specified otherwise, all units of length are in mm.

Take Figure 3.5 for example - the above is a combination of tracking and geometry navigator verbosity printing information about a secondary photon in the familiar copper plate geometry from earlier in this report.

In the zeroth step, information about this newly-created secondary is printed to screen and dynamic quantities such as its safety are calculated by the `G4Navigator` class - which subsequently invokes its `ComputeStep` method; computing the distance to the next boundary along the direction vector of the secondary. Part of this computation involves passing a proposed physics step (determined by well-defined probabilities for various processes to occur) comparing it to safety. If safety is larger than the proposed step as in Figure 3.5, the proposed step will be taken. This is consistent with the change in position from `Step#0` and `Step#1`, as the secondary appears to move 23 μm along the x-axis. Subtracting `Safety` from the x-component of `GlobalPoint`, we observe that,

$$-1.33888 - 48.66190 = -50.00078 \text{ mm, or}$$
$$\approx -5 \text{ cm.}$$

In other words, adding the position of a secondary with its safety returns half the

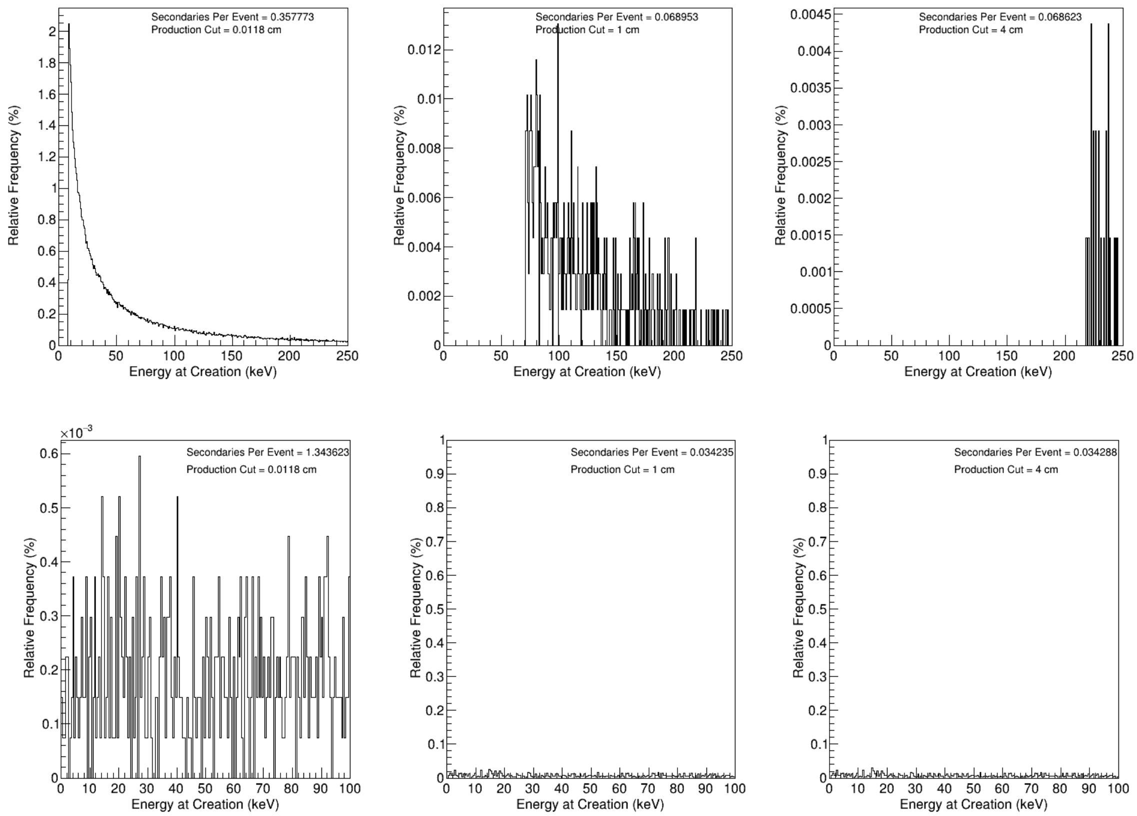

Figure 3.6: Geant4: Histograms showing (top row) energy of neutral secondaries and (bottom row) energy of charged secondaries with the same geometry and set of cuts as for Figures 3.2 and 3.3, but instead using Geant4's standard electromagnetic physics list, option 1.

length of the copper absorber. This exactly what we would expect if safety gives the distance to the nearest volume boundary. The above calculation has been verified for numerous geometries, primary energies, gun positions, and physics lists (including standard electromagnetic physics, option 1); each scenario similarly suggests that safety is calculated correctly in TestEm5. A similar investigation has not been performed outside of TestEm5, so it remains to be seen if this result is consistent across Geant4's entire framework.

3.3.2 The `ApplyCuts` Flag

Each standard electromagnetic physics list is designed to offer varying levels of simulation speed in exchange for different levels of detail. The standard electromagnetic physics list, option 1 is described in the documentation as being fast but less accurate. This description mentions an `ApplyCuts` flag which may be toggled on via the `SetApplyCuts` method as an instance of the `G4EmParameters` class in a physics list constructor.

The difference between this flag and the boolean `ApplyCut` data member that was used to define condition 3.3 is ambiguous in the Geant4 documentation. However, given that this physics list offers a reduced simulation time, it may be reasonable to assume that the above flag could influence the way that production cuts behave.

Investigating their difference further, a similar test as in Figures 3.2 and 3.3 was performed using Geant4's standard electromangetic physics list, option 1. This difference is crucial, as option 4 (the list that TestEm5 uses natively) does not toggle this flag on in its constructor. Figure 3.6 illustrates the results obtained from carrying out this test.

Qualitatively, the results do not differ significantly from those obtained in the previous section; neutral secondaries below the production threshold (and now above!) are cut indiscriminately and there is a diminished but non-zero rate of charged secondary production. Neutral secondaries not appearing above the production threshold may be caused by the physics list's less sophisticated bremsstrahlung model, which could affect the rate of production of photons in continuous processes. Also note that the range-to-energy conversions in option 1 and option 4 do not differ by more than 1 keV for a given production cut, so inconsistent production thresholds are not why a difference is observed.

Quantitatively, the spectra differ significantly. This is because option 1 for standard electromagnetic physics is overall less accurate than option 4, given that the former uses simplified models for Compton scattering and the photoelectric effect - two of the primary production mechanisms for secondaries in the energy range of interest. This is also why no $\sim$ 8 keV excitation line is observed in copper - the Compton scattering model employed by option 4 also features a more sophisticated atomic de-excitation model.

From the above histograms, it is clear that toggling the `ApplyCuts` flag does not have a qualitatively different effect on how production cuts interact with safety than what has been observed previously. While both the `ApplyCut` or `ApplyCuts` flag have a similar effect on the observed spectra, the precise difference between them (if any) warrants further clarification.

3.3.3 Charged Primaries

The effects of shooting 2 MeV electrons in the copper plate geometry were briefly explored. The spectra of secondary energies shown in Figure 3.7 strongly resembles those observed in Figures 3.2 and 3.3. Notice that a minuscule production cut is applied in the leftmost distribution just below the 8.05 keV x-ray line in copper to reduce runtime. The qualitative features of each spectrum remain unaffected.

In spite of the small attenuation length of a 2 MeV electron in copper ($\sim$ 1.5 mm, according to the table of registered couples), there are several processes through which primary electrons may produce photons. This is evidenced by the upper-left histogram of Figure 3.7, which shows that approximately 13 secondary photons are generated per primary electron. Since photons have a significantly larger attenuation length than electrons in copper, similar behaviour is expected as for the case with neutral primaries.

This provides compelling evidence that the behaviour of production cuts and

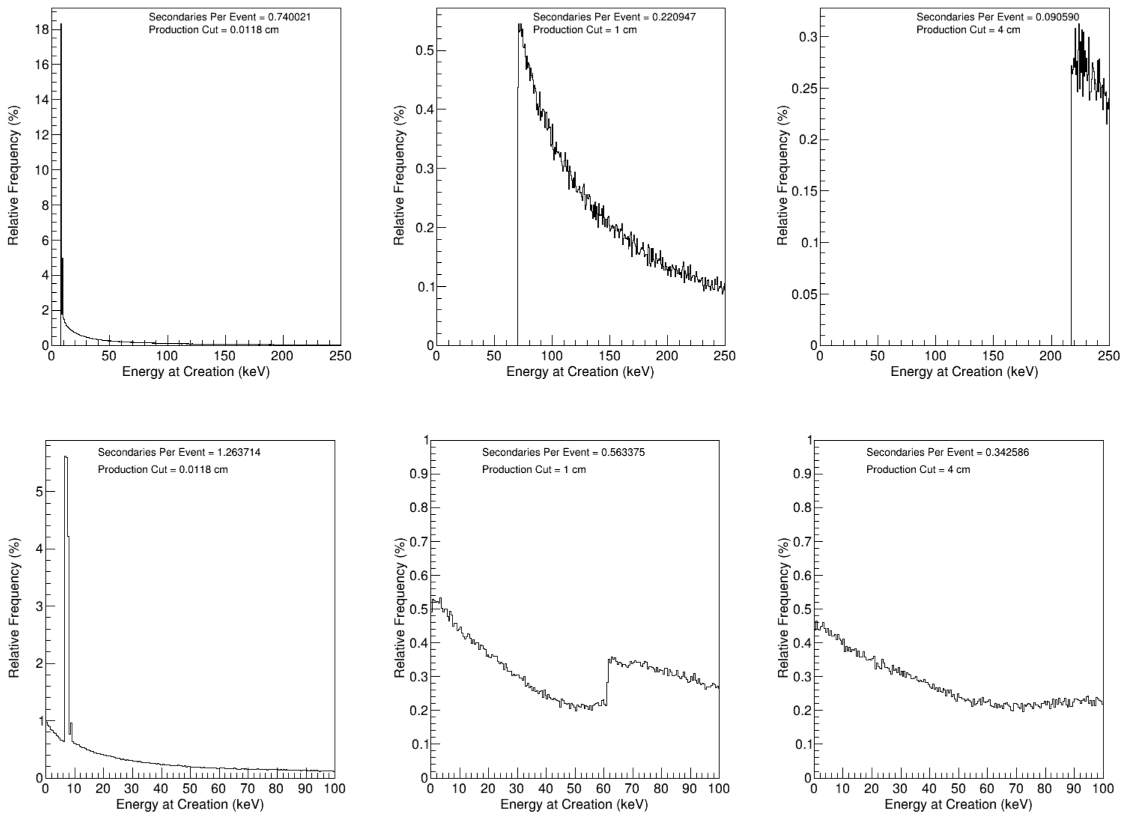

Figure 3.7: Geant4: Histograms showing the energy at creation of neutral (top) and charged (bottom) secondaries in a 10 cm thick copper absorber resulting from 10^6 incident electrons carrying an energy of 2 MeV with (left) a 118 μm production cut, (middle) a 1 cm production cut, and (right) a 4 cm production cut. A production threshold of 1 cm in copper is equivalent to an electron energy of 14.6 MeV, whereas a threshold of 4 cm is equivalent to an electron energy of 74.0 MeV. The number of secondaries per event is given by the quotient of the number of secondaries created and number of incident primaries.

safety is not influenced by the charge of incident primaries.

3.4 Next Steps

Given that safety is calculated correctly for electromagnetic processes, a continuation of this investigation should include attempts to locate where condition 3.3 is implemented in the Geant4 source code. It is suggested in the documentation that comparisons between safety and production cuts are handled by the tracking manager.

Additionally, it would be interesting to explore if the observed behaviour of safety is consistent across higher energy ranges. Given that Geant4 was designed with high-energy applications in mind, it is possible that this issue is a product of the relatively low energy range that has been considered. If this is the case, then at what energies to we observe a difference, and where in the source code is this handled?

Finally, if the source of this issue cannot be found, an appropriate set of cuts for each region in the SuperCDMS detector geometry should be developed. Since the goal of this investigation is to optimize simulation efforts for the collaboration, using SuperSim to determine a list of cuts per region that does not significantly alter background signals while simultaneously decreasing CPU time would be productive.

Chapter 4

Discussion and Conclusion

This report sought to investigate the effects of different exposure and cooldown times on the background rate originating from cosmogenic activation in the SuperCDMS SNOLAB experiment. Assuming a SLE exposure of 1270 days at the time that the bulk of the experiment's copper instrumentation goes underground, it was found through Monte Carlo simulation that any additional cooldown time would not produce an appreciable background rate reduction. This report therefore recommends that the collaboration increase the allotment for material internal activation of the SuperCDMS SNOLAB experiment to a conservative 15% of the total observed rate while looking to reduce event rates originating from other sources of background.

It is important to emphasize that the reliability of the results in this investigation are limited by two factors: first, a comprehensive assay of each copper piece in the cryostat would greatly help to inform if the assumptions of cosmic ray exposure are realistic. Secondly, location and time-specific cosmic ray neutron and proton flux parameterizations, such as those provided in ref. [31], would complement the previous point; geography-specific cosmic ray fluxes would signal a departure from the assumption that all exposure occurs at sea-level and contribute to the realism of any assumptions on radionuclide production rates.

Secondarily, this report aimed to confirm and troubleshoot an issue with Geant4's production cuts mechanism. It was first found that Geant4's "safety" mechanism is calculated in a way that is consistent with the documentation. This means that the issue is not caused by safety being calculated incorrectly.

Subsequent investigations using `TestEm5` revealed that production cuts do not behave as advertised in the Geant4 documentation for *electromagnetically neutral* secondary particles. However, they behave as expected for charged secondaries. The cause of this issue remains unknown. A thorough investigation of each standard electromagnetic physics list that ships with the simulations platform is recommended; different lists include flags - such as the `ApplyCuts` flag - whose purpose is ambiguous in the documentation.

It is strongly recommended that a follow-up investigation be conducted before the next DMC production cycle, as more efficient neutral secondary modelling has the potential to greatly reduce runtimes on this resource-intensive component of the simulations production chain.

References

[1] Georges Aad et al. Observation of a new particle in the search for the Standard Model Higgs boson with the ATLAS detector at the LHC. *Phys. Lett. B*, 716:1–29, 2012.

[2] K. Abe et al. Observation of large cp violation in the neutral b meson system. *Physical Review Letters*, 87(9), August 2001.

[3] R. Agnese et al. Projected sensitivity of the supercdms snolab experiment. *Physical Review D*, 95(8), April 2017.

[4] R. Agnese et al. Production rate measurement of tritium and other cosmogenic isotopes in germanium with cdmslite. *Astroparticle Physics*, 104:1–12, 2019.

[5] S. Agostinelli et al. Geant4—a simulation toolkit. *Nuclear Instruments and Methods in Physics Research Section A: Accelerators, Spectrometers, Detectors and Associated Equipment*, 506(3):250–303, 2003.

[6] B. Aharmim et al. Cosmogenic neutron production at the sudbury neutrino observatory. *Physical Review D*, 100(11), December 2019.

[7] M. F. Albakry et al. A strategy for low-mass dark matter searches with cryogenic detectors in the supercdms snolab facility, 2023.

[8] M.F. Albakry et al. Search for low-mass dark matter via bremsstrahlung radiation and the migdal effect in supercdms. *Physical Review D*, 107(11), June 2023.

[9] J. Allison et al. Geant4 developments and applications. *IEEE Transactions on Nuclear Science*, 53(1):270–278, 2006.

[10] J. Allison et al. Recent developments in geant4. *Nuclear Instruments and Methods in Physics Research Section A: Accelerators, Spectrometers, Detectors and Associated Equipment*, 835:186–225, 2016.

[11] A. Arbey and F. Mahmoudi. Dark matter and the early universe: A review. *Progress in Particle and Nuclear Physics*, 119:103865, July 2021.

[12] S. Cebrián. Cosmogenic activation of materials. *International Journal of Modern Physics A*, 32(30):1743006, October 2017.

[13] Serguei Chatrchyan et al. Observation of a New Boson at a Mass of 125 GeV with the CMS Experiment at the LHC. *Phys. Lett. B*, 716:30–61, 2012.

[14] Douglas Clowe et al. A direct empirical proof of the existence of dark matter. *The Astrophysical Journal*, 648(2):L109–L113, August 2006.

[15] Jodi Cooley. Dark matter direct detection of classical wimps. *SciPost Physics Lecture Notes*, May 2022.

[16] E. Corbelli and P. Salucci. The extended rotation curve and the dark matter halo of m33. *Monthly Notices of the Royal Astronomical Society*, 311(2):441–447, January 2000.

[17] A. Elersich et al. Study of cosmogenic activation above ground for the darkside-20k experiment. *Astroparticle Physics*, 152:102878, 2023.

[18] Jonathan L. Feng. Dark matter candidates from particle physics and methods of detection. *Annual Review of Astronomy and Astrophysics*, 48(1):495–545, August 2010.

[19] Héctor Gisbert and Antonio Pich. Direct cp violation in $K^0 \to \pi\pi$: Standard model status. *Reports on Progress in Physics*, 81(7):076201, June 2018.

[20] M.S. Gordon et al. Measurement of the flux and energy spectrum of cosmic-ray induced neutrons on the ground. *IEEE Transactions on Nuclear Science*, 51(6):3427–3434, 2004.

[21] J.H. Hubbell and S.M. Selzter. X-ray mass attenuation coefficients, July 2024.

[22] Lam Hui. Wave dark matter. *Annual Review of Astronomy and Astrophysics*, 59(1):247–289, 2021.

[23] P.N. Luke et al. Calorimetric ionization detector. *Nuclear Instruments and Methods in Physics Research Section A: Accelerators, Spectrometers, Detectors and Associated Equipment*, 289(3):406–409, 1990.

[24] D.-M. Mei et al. Muon-induced background study for underground laboratories. *Physical Review D*, 73(5), March 2006.

[25] D.-M. Mei et al. Cosmogenic production as a background in searching for rare physics processes. *Astroparticle Physics*, 31(6), July 2009.

[26] Mihaly Novak. Electromagnetic physics: special em topics, September 2020.

[27] Leszek Roszkowski et al. Wimp dark matter candidates and searches—current status and future prospects. *Reports on Progress in Physics*, 81(6):066201, May 2018.

[28] V.C. Rubin et al. Rotational properties of 21 SC galaxies with a large range of luminosities and radii, from NGC 4605 (R=4kpc) to UGC 2885 (R=122kpc). *The Astrophysical Journal*, 238:471–487, June 1980.

[29] Vera C. Rubin and Jr. Ford, W. Kent. Rotation of the Andromeda Nebula from a Spectroscopic Survey of Emission Regions. *The Astrophysical Journal*, 159:379, February 1970.

[30] B. Ryden. *Introduction to cosmology.* Cambridge University Press, 1970.

[31] Tatsuhiko Sato. Analytical model for estimating terrestrial cosmic ray fluxes nearly anytime and anywhere in the world: Extension of parma/expacs. *PLoS ONE*, December 2015.

[32] M. Schumann. Direct detection of wimp dark matter: concepts and status. *Journal of Physics G: Nuclear and Particle Physics*, 46(10):103003, August 2019.

[33] Stefaan Tavernier. *Experimental Techniques in Nuclear and Particle Physics.* Springer, 2010.

[34] Albert C. Thompson et al. X-ray data booklet, January 2001.

[35] M. Thomson. *Modern particle physics.* Cambridge University Press, New York, 2013.

[36] R. L. Workman et al. Review of Particle Physics. *Progress of Theoretical and Experimental Physics*, 2022(8):083C01, August 2022.

[37] F. Zwicky. Nebulae as gravitational lenses. *Phys. Rev.*, 51:290, 1937.

Appendix A
Derivation of Activity Formula for Cosmogenic Isotopes

We begin by noting that the number of atoms induced via cosmogenic activation per unit time may be expressed as:

$$\frac{dN}{dt} = R_i - \frac{N}{\tau}, \tag{A.1}$$

where R_i is the production rate and τ is the lifetime of some nuclide i in the material. Dropping subscripts and solving for the number of activated atoms via separation of variables,

$$\begin{aligned} \int \frac{dN}{R - \frac{N}{\tau}} &= \int dt \\ -\tau \ln \left| R - \frac{N}{\tau} \right| &= t + C, \end{aligned}$$

where C is a constant of integration. To isolate N, we must take the exponent of both sides,

$$\begin{aligned} R - \frac{N}{\tau} &= e^{-\frac{t+C}{\tau}} \\ N(t) &= \tau(R - e^{-\frac{t+C}{\tau}}). \end{aligned} \tag{A.2}$$

Assuming the target material is initially pure until its purchase (i.e., until the collaboration is able to track its exposure history), permits the imposition of the condition $N(t = 0) = 0$. Therefore,

$$\begin{aligned} N(0) = 0 &= \tau \left(R - e^{-\frac{C}{\tau}} \right) \\ e^{-\frac{C}{\tau}} &= R. \end{aligned}$$

Inserting this into equation A.2 yields:

$$\begin{aligned} N(t) &= \tau \left(R - Re^{-\frac{t}{\tau}} \right) \\ N(t) &= \tau R \left(1 - e^{-\frac{t}{\tau}} \right). \end{aligned} \tag{A.3}$$

Equation A.3 gives the number of cosmogenic isotopes with lifetime τ present in a sample if they are produced at a constant rate R for some time t. Though, it still does not tell the whole story; cosmogenic isotopes will continue to decay once they are underground and cosmogenic activation has effectively ceased! Therefore, we must include an additional factor to reflect this:

$$N(t) = \tau R \left(1 - e^{-\frac{t_{\exp}}{\tau}}\right) e^{-\frac{t}{\tau}}, \tag{A.4}$$

where the exposure time is now treated as a constant. The variable t represents a *cooldown time*, which refers to the period of time between a component's arrival underground and its integration into the experiment.

In order to recover the formula for activity from A.4, we simply take the negative of its derivative with respect to t, as per definition 2.1:

$$A(t) = R \left(1 - e^{-\frac{t_{\exp}}{\tau}}\right) e^{-\frac{t}{\tau}}. \tag{A.5}$$

More interesting for a background study is the average activity over some period of time. This quantity permits the calculation for an expected number of events over a specific runtime, which facilitates obtaining validations and background estimates. To find the average activity, we simply integrate A.5 and divide by the difference between each bound of integration:

$$A_{avg}(t_1, t_2) = \frac{1}{t_2 - t_1} \int_{t_1}^{t_2} A(t),$$

letting $t_2 - t_1 = \Delta t$,

$$\begin{aligned} A_{avg}(t_1, t_2) &= \frac{R}{\Delta t} \left[1 - e^{-\frac{t_{\exp}}{\tau}}\right] \int_{t_1}^{t_2} e^{-\frac{t}{\tau}} \\ &= \frac{\tau R}{\Delta t} \left[1 - e^{-\frac{t_{\exp}}{\tau}}\right] \left[e^{-\frac{t_1}{\tau}} - e^{-\frac{t_2}{\tau}}\right]. \end{aligned} \tag{A.6}$$

One can also use the well-known identity $\tau = \lambda / \ln(2)$, to express the above in terms of an isotope's half-life, λ:

$$A_{\text{avg}}(t_1, t_2) = \frac{\lambda R}{\ln(2)\Delta t} \left[1 - 2^{\frac{-t_{\exp}}{\lambda}}\right] \left[e^{-\frac{t_1}{\lambda}} - e^{-\frac{t_2}{\lambda}}\right]. \tag{A.7}$$

We can also express equation A.6 in more suggestive notation:

$$A_{\text{avg}}(t_{\text{exp}}, t_{\text{cool}}, t_{\text{run}}) = \frac{\tau R}{t_{\text{run}}} \left[1 - e^{-\frac{t_{\exp}}{\tau}}\right] \times \left[e^{-\frac{t_{\text{cool}}}{\tau}} - e^{-\frac{t_{\text{cool}} + t_{\text{run}}}{\tau}}\right]. \tag{A.8}$$

Appendix B
Calculation of Median Compton Scattering Angle

This section, consistent with the rest of this report, uses natural units: c = h = 1.

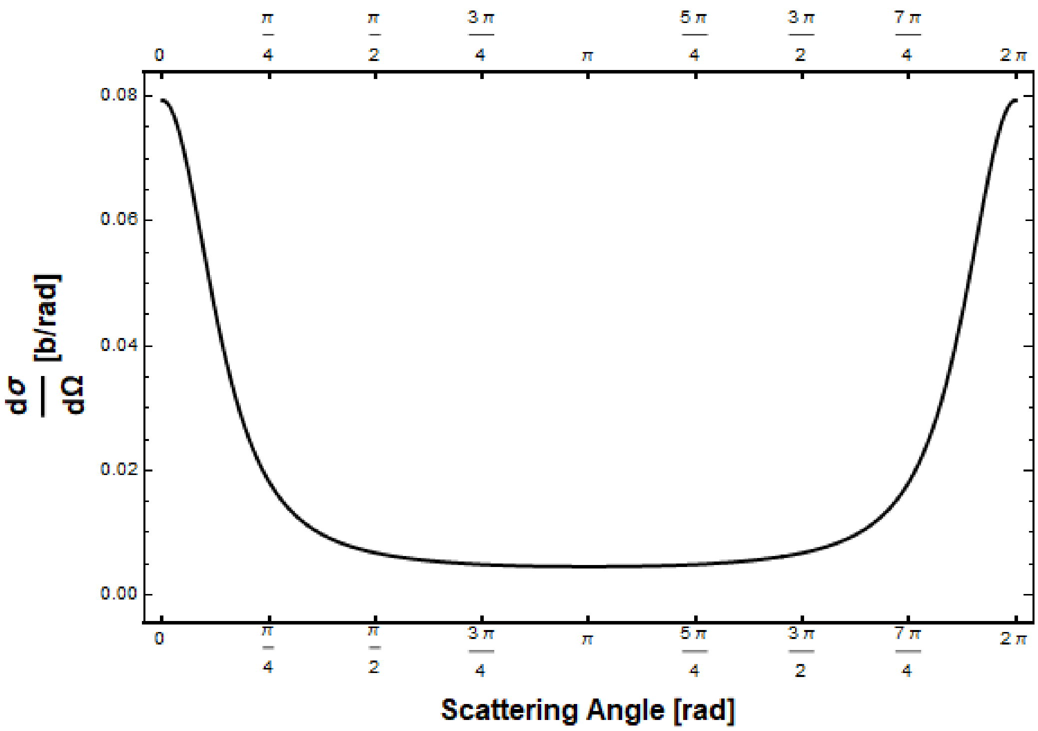

Figure B.1: Mathematica plot of the differential cross section for a 2 MeV incident photon undergoing Compton scattering as a function of its scattering angle.

We begin with the Klein-Nishima formula for an unpolarized photon:

$$\frac{d\sigma}{d\Omega} = \frac{1}{2} r_e^2 \left(\frac{\lambda}{\lambda'}\right) \left[\frac{\lambda}{\lambda'} + \frac{\lambda'}{\lambda} - \sin^2(\theta)\right], \tag{B.1}$$

where $r_e = 2.82$ fm is the classical electron radius, λ/λ' is the ratio of wavelengths of initial and scattered photons (see equation B.2), and θ is the scattering angle. Recall that the difference in wavelengths of an incoming photon and a scattered photon in Compton scattering is given by:

$$\lambda' - \lambda = \frac{1}{m_e}[1 - \cos(\theta)]. \tag{B.2}$$

We want to recover an expression for the ratio of both wavelengths. To proceed, we divide both sides by λ:

$$\frac{\lambda'}{\lambda} = 1 - \frac{1}{m_e\lambda}[1 - \cos(\theta)].$$

Then, recalling that $E_\gamma = 1/\lambda$ in natural units,

$$\frac{\lambda'}{\lambda} = \frac{m_e - E_\gamma[1 - \cos(\theta)]}{m_e}.$$

Finally, we take the inverse of both sides and factor out m_e:

$$\frac{\lambda}{\lambda'} = \frac{m_e}{m_e - E_\gamma[1 - \cos(\theta)]}$$
$$\frac{\lambda}{\lambda'} = \frac{1}{1 - (E_\gamma/m_e)[1 - \cos(\theta)]} \tag{B.3}$$

Using B.3, we arrive at the differential cross section of an unpolarized 2 MeV photon as a function of its scattering angle with an electron which is plotted in Figure B.1.

In order to find the median Compton scattering angle, a crude brute force method is employed using Wolfram Mathematica. First, equation B.1 is integrated over the domain [0,π]. Then, another integral is taken over a small domain, [0,ϵ], and it is divided by the first result. Successively larger integrals are taken until the quotient of both integrals gives 1/2. In other words, this quotient represents the angle at which there is an equal probability of an inbound photon scattering above or below it.

Using this method, we obtain $\theta_{\text{median}} \sim 49.7^\circ$ for the median Compton scattering angle of a 2 MeV photon. It is then possible to use θ_{median} to compute the median energy of photons which undergo Compton scattering. This helps to inform us on where Compton scatters need to occur in an absorber for them to be within safety (see Section 3.2).